Smart bricks for seismic assessment of masonry structures though Kriging strain reconstruction: A numerical study.

Enrique García-Macías[a,*], Filippo Ubertini[b]

[a]*Department of Continuum Mechanics and Structural Analysis, School of Engineering, Universidad de Sevilla, Spain*
[b]*Department of Civil and Environmental Engineering, University of Perugia, Via G Duranti 93, Perugia 06125, Italy*

Highlights

- Installation conditions of smart bricks are numerically investigated
- Birth and death elements are used to simulate smart bricks installation
- A Kriging interpolation-based damage detection is proposed
- The seismic behavior of a masonry building equipped with smart bricks is studied

Abstract

The intrinsic vulnerability of masonry structures to seismic events makes Structural Health Monitoring of the utmost importance for the conservation of the built heritage. The development of piezoresistive bricks, also termed smart bricks, is an innovative technology recently proposed by the authors for the monitoring of such structures. The smart bricks exhibit measurable variations in their electrical properties when subjected to external loads or, alternatively, strain self-sensing capabilities. Therefore, the deployment of a network of smart bricks into a masonry structure confers self-diagnostic properties to the host structure. In this light, this paper presents a theoretical investigation on the application of smart bricks to full-scale masonry structures for seismic assessment. In particular, the numerical tests are first aimed at studying the effects of different operating conditions of smart bricks. This includes the study of the convenience of providing electrical isolation conditions to the sensors, as well as the effectiveness of smart bricks installed into existing structures. Secondly, numerical results are presented on the seismic analysis of a three-dimensional masonry building equipped with a network of smart bricks. In order to map the strain field throughout the structure exploiting the outputs of a limited number of sensors, a Kriging interpolation-based strain reconstruction approach is proposed. The paper presents valuable conclusions on the design of monitoring systems composed by smart bricks, and the numerical results demonstrate the potential application of the proposed Kriging interpolation-based approach for damage detection and localization in masonry structures.

Keywords: Masonry structures, Smart bricks, Piezoresistivity, Structural Health Monitoring, Damage detection, Kriging interpolator

1. Introduction and research aim

There is a strong consciousness of the importance of preserving historic buildings as vital pieces of the cultural, historical and artistic heritage. Particularly, the assessment of the health condition and conservation of masonry structures, which constitute a large portion of the heritage assets, is of primary concern due to their intrinsic vulnerability to aging deterioration and natural catastrophes [1]. Recent severe seismic events such as the magnitude-6.2 earthquake of Amatrice (Italy) in 2006 [2] caused the partial or total collapse of a large portion of the masonry buildings in the historical center of the municipality [3]. This has motivated the implementation of numerous Structural Health Monitoring (SHM) systems [4, 5]. SHM encompasses the application of Non-Destructive Testing (NDT) and damage detection that enable the automated assessment of the integrity of structures and allow an effective condition-based maintenance [6]. Experiences on the monitoring of diverse historic structures, including bridges [7, 8], towers [9], churches [10] or municipal buildings [5], have demonstrated the great potential of SHM for heritage preservation and restoration.

*Corresponding author.
Email address: egarcia28@us.es (Enrique García-Macías)

A variety of sensing technologies has been applied to the SHM of masonry structures. Lots of attention has been devoted to ambient vibration-based monitoring, which allows the estimation of the modal features of structures through a limited number of accelerometers [11]. In this context, the appearance of damages can be correlated to changes in the resonant frequencies or modes of vibration [12, 13], as well as to variations in short-term damping measurements [14]. On the basis of dynamic measurements, diverse damage localization approaches have been proposed in the literature. Ramos *et al*. [15] investigated different dynamic-based methods for damage localization in laboratory masonry arches under ambient vibration and random impact excitations. Although such approaches are effective in assessing the global state of structures, local or incipient damages that do not manifest in the global response may go unnoticed [6]. The monitoring of static parameters, such as strains, tilts or displacements, offers an alternative for assessing the performance of structures and tracking local changes that are often hardly observable by dynamic-based monitoring. There exist different approaches depending on the desired outcomes [16, 17]. Linear Variable Displacement Transducers (LVDTs) are usually employed in masonry structures for the monitoring of crack amplitudes and their evolution in time [18]. Flat-jacks offer a moderately destructive test to assess the local vertical stresses and local elastic modulus of masonry [19]. Concerning contactless sensing technologies, Lubowiecka *et al*. [20] used laser scanning to accurately reconstruct the geometry of a medieval masonry bridge and Ground Penetrating Radar (GPR) to investigate its internal structure. Ghorbani *et al*. [21] used three-dimensional Digital Image Correlation (DIC) to measure surface deformation fields on full-scale masonry walls and define crack patterns. Sonic tests are also widely used to estimate the stiffness of masonry, including the detection of voids and cracks [22]. Another popular non-contact technique is represented by infrared thermography which allows identifying damages through irregularities in the surface temperature distributions of structures [23]. Fiber Bragg Grating sensors (FBG) provide distributed strain measurements that permit to detect the appearance of damages throughout proper processing [24]. While promising, these pose problems in terms of architectural invasiveness and long-term reliability.

Recent advances in the fields of Materials Science and Nanotechnology have enabled the development of novel nano- or micro-modified self-sensing composites with a vast potential for SHM applications [25, 26]. These smart composites are commonly enriched with carbon-based fillers, such as carbon black, carbon nanofibers, carbon nanotubes or graphene [27]. The addition of small concentrations of such fillers to cement-based or polymer materials has been reported to confer self-sensing properties to the resulting composite [28, 29]. In virtue of these new capabilities, the composites output measurable variations in their electrical properties when subjected to mechanical deformations, that is a piezoresistive behavior [28, 29]. Therefore, these innovative materials not only fulfill a structural function, but it is also possible to exploit their strain-sensitivity for condition-based maintenance and decision making in structural retrofitting [27, 30]. Intrinsic self-sensing cement-based composites, often termed "smart concretes", have been shown particularly promising in civil infrastructures due to their similarity with conventional concrete [31, 32]. Applications of smart concretes comprise the development of integral smart structures [33, 34], embedded strain sensors [35, 36], as well as superficial sensors or smart skins [37]. Also promising are the self-sensing polymer composites for the development of large surface strain sensors and stretchable electronics [38–40]. Although many authors have striven to apply smart materials to concrete or aerospace structures, the number of attempts to bring this concept to masonry structures is very scarce. A first approximation was done by Engel *et al*. [41] who proposed inserting a conventional tripe axis accelerometer into masonry bricks. Nevertheless, the concept of self-sensing structural masonry was first proposed by Downey *et al*. [42] who manufactured piezoresistive burned clay bricks doped with titanium dioxide, termed "smart bricks". The authors demonstrated the potential of this innovative technology for crack detection applications on a small-scale masonry wall equipped with three inserted smart bricks. While promising, the application of this technology into full-scale masonry structures is yet to defined. Furthermore, the development of theoretical approaches that aid at interpreting the output of the sensors and tailoring their position still needs to be addressed.

In this paper, a theoretical investigation on the application of smart bricks to full-scale masonry structures for seismic assessment is presented. In particular, the contributions of this work are two-fold: (i) analysis of operational conditions of smart bricks deployed into a masonry structure, and (ii) damage detection and localization based on strain mapping. Firstly, this work is aimed at evaluating the need for electrical isolation of the bricks, as well as the effectiveness of smart bricks deployed into pre-existing masonry structures. To this end, the electrical output of smart bricks is computed through an electromechanical Finite Element (FE) simulation. The numerical results demonstrate that electrically isolated smart bricks exhibit more sensitive responses. Moreover, the results show that smart bricks deployed into a pre-existing structure can monitor variable load conditions. Secondly, a damage detection/localization approach is proposed for monitoring systems with sensor networks of smart bricks. Typically, strain-based SHM systems demand dense sensor networks to achieve high-resolution strain maps and enable damage detection. Nevertheless, the monitoring of heritage structures requires minimally invasive interventions and, consequently, sensors must be limited in number. In this paper, the Kriging interpolator is proposed to map the strain throughout the monitored structure with a relatively limited number of smart bricks. The proposed

damage detection approach is tested in a numerical FE model of a masonry building. The investigation comprises both pushover analyses and direct-time integration of the structure under ground accelerations.

The paper is organized as follows. Section 2 introduces the concept of smart bricks and their application to SHM of masonry structures. Section 3 presents the electromechanical modeling of smart bricks. Section 4 details the mathematical formulation of the Kriging interpolator and introduces the proposed damage detection/localization approach. Section 5 presents the numerical results and, eventually, Section 6 concludes the paper.

2. Smart bricks for SHM applications

Smart bricks were first defined by Downey *et al*. [42] as piezoresistive burned clay bricks that exhibit self-sensing capabilities through measurable changes in their electrical resistance when subjected to external loads. Their experimental results demonstrated that conventional clay bricks, that is to say neat bricks, already meet this definition and can be used as piezoresistive sensors for strain monitoring. In order to enhance their mechanical and conductivity properties, those authors enriched neat bricks with titanium dioxide ($Ti0_2$) particles. Other types of additives could be also used such as fire-resistant metals, or carbon-based particles with low baking temperatures.

On this basis, Fig. 1 schematizes a possible monitoring layout for a masonry structure equipped with smart bricks for SHM. This consists of the deployment of a certain number of smart bricks into the sections of interest, such as façades or key locations with load concentrations at connections, lintels or openings. The smart bricks act as mechanically robust sensors with similar stiffness to the rest of brick units in the structure. The sensing capability of the smart bricks is exploited through variations of their electrical resistance. Hence, the measurement setup at every smart brick can follow the principles of conventional resistivity testing, with both two- or four-probe electrode layouts. To do so, two or four electrodes must be embedded in the smart bricks in such a way that a potential difference can be applied between them. Afterward, the electrical outputs of the sensors are sent to a computer terminal to perform data acquisition and on-site data processing. Finally, the information is sent to a server to perform further post-processing. In this paper, the Kriging interpolator is proposed to reconstruct the strain map throughout the structure, whereby damages can be detected from load-path changes or anomalous strain concentrations or releases.

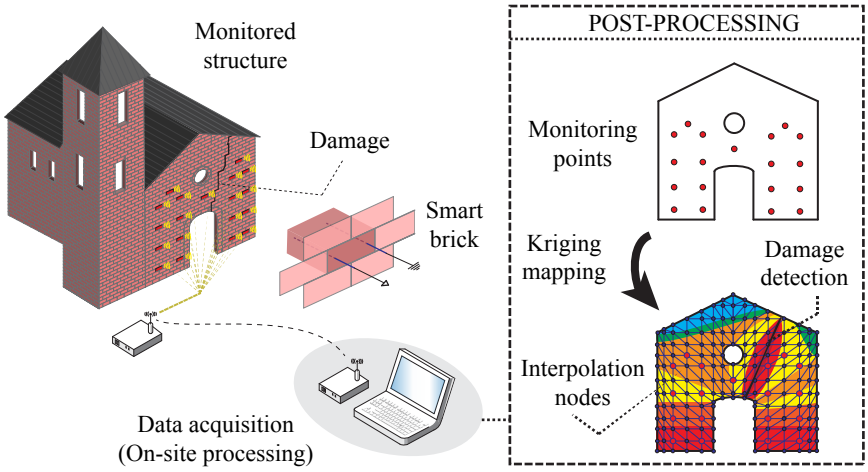

Figure 1: Schematic of SHM system architecture with smart bricks.

This technology outperforms conventional off-the-shelf sensors since smart bricks form part of the structure itself. Hence, masonry equipped with smart bricks behaves as a self-diagnostic structure and provides high-fidelity information on its strain state. In addition, smart bricks mimic the reliability of conventional masonry and, therefore, these have a great potential for long-term monitoring applications. Finally, a fundamental feature of this technology relates to the aesthetic appearance of smart bricks, which is essentially the same as conventional bricks. This aspect is essential for the monitoring of heritage buildings where the aesthetic impact of interventions must be minimal. Moreover, the electrodes and electronic circuitry can be hidden in the inner part of the walls or within the mortar layers.

3. Electromechanical modeling of smart bricks deployed into masonry structures

3.1. Adopted modeling approaches for masonry

Depending on the level of accuracy and simplicity desired, three different numerical representations of masonry are commonly used in the literature [43, 44], namely micro-modeling, simplified micro-modeling, and macro-modeling (Fig. 2). In the micro-modeling approach, brick units and mortar are modeled using different continuum elements accounting for their elastic and inelastic properties along with failure criteria [45, 46]. Additionally, interfaces also represent potential crack/slip planes defined by the properties of joint failure under normal and shear contact stresses. Although such approaches offer a highly faithful representation of masonry, convergence issues and high computational costs arise due to the elevated number of contact surfaces. Next in simplicity are the simplified micro-modeling approaches. These lump brick/mortar interfaces and mortar thickness into zero thickness interfaces, while the units are expanded in order to keep the geometry unchanged [44, 47–51]. Therefore, masonry is idealized as a set of blocks connected by potential fracture/slip joints, what implies a considerable reduction of the number of contact surfaces. The last and least computationally expensive technique corresponds to macro-modeling approaches. In this technique, units, mortar and unit-mortar interfaces are smeared out in a continuum element. Given that this neglects any unit-mortar interface, macro-modeling approaches limit to representing the global failure mechanisms of masonry. In order to compute the equivalent properties of the macro-element, the most commonly used technique consists of the homogenization of periodic cells of masonry [52]. This process is generally performed in two steps, introducing head (or vertical) and bed (or horizontal) joints successively. Macro-modeling approaches are well-suited to analyze the global response of masonry structures, where the use of micro- or simplified micro-modeling would entail exorbitant computational costs.

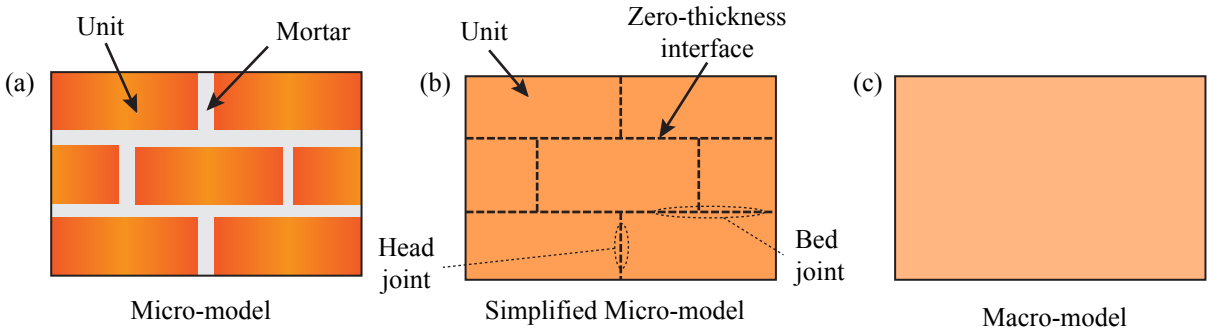

Figure 2: Modeling strategies for masonry structures: (a) micro-modeling, (b) simplified micro-modeling, and (c) macro-modeling.

In this research work, the numerical tests comprise the analysis of a masonry shear wall and a three-dimensional masonry building. In the former case, the three modeling approaches for masonry structures are employed depending on the focus of interest. Conversely, only the macro-modeling approach is used for the analysis of the full-scale masonry building to avoid excessive computational costs. All the numerical simulations are conducted in the commercial Finite Element (FE) code ANSYS v15.0 [53].

In the detailed micro-modeling, both the brick units and mortar layers are modeled with the eight-nodes SOLID65 brick elements with three translational Degrees of Freedom (DOFs) per node. This element follows the Willian-Warnke yield criterion [54] for brittle materials, being capable of cracking in tension and crushing in compression. The presence of a crack at an integration point is considered through a modification of the stress-strain relations, introducing a plane of weakness in the direction normal to the crack. Also, a shear transfer coefficient, β_t, is introduced to account for a shear strength reduction in those cracked elements sustaining sliding. If the crack closes, then compressive stresses are transmitted across the crack plane. A second shear transfer coefficient, β_c, is also defined for closed cracks. Furthermore, the smeared crack approach is combined with the elastic-perfectly plastic Drucker-Prager model to simulate the nonlinear behavior of masonry elements.

In the case of simplified micro-modeling, the Cohesion Zone Material (CSM) model with critical fracture energy is used to model the zero thickness brick-mortar interfaces. CSM models allow for simulating debonding in normal direction and sliding in the tangential direction. Due to shrinkage of poorly cured mortar or improper filling, head joints often exhibit lower contact stiffness in practice. Because of this, head and bed joints are modeled independently, considering lower opening stiffness in the former as suggested by Li *et al.* [50].

Finally, homogeneous macro elements are utilized for the modeling of the full-scale masonry building. In a similar way to the previous approaches, the combination of the Drucker-Prager plasticity model and the smeared

crack approach is used to simulate the macroscopic behavior of masonry. Hence, the numerical simulations in this case are unaimed at exploring local effects in the brick-mortar interfaces, but rather they are aimed at providing a reasonably inexpensive computational tool for investigating the global failure mechanisms of the building.

3.2. Adopted modeling approach for smart bricks

On the basis of the previous prescriptions on the simulation of masonry structures, the modeling of smart bricks requires the incorporation of their piezoresistive behavior. To do so, it is necessary to link the equations related to the electrical behavior of the material with those describing the mechanical strain state. The electrical resistivity matrix, $\boldsymbol{\rho}$, relates the current intensity vector, $\boldsymbol{J}$, to the electric field vector, $\boldsymbol{E}$, as $\boldsymbol{E} = \boldsymbol{\rho}\boldsymbol{J}$. This relation can be written in matrix notation as:

$$\begin{bmatrix} E_1 \\ E_2 \\ E_3 \end{bmatrix} = \begin{bmatrix} \rho_1 & \rho_6 & \rho_5 \\ \rho_6 & \rho_2 & \rho_4 \\ \rho_5 & \rho_4 & \rho_3 \end{bmatrix} \begin{bmatrix} J_1 \\ J_2 \\ J_3 \end{bmatrix} \tag{1}$$

When the smart brick is not subjected to any mechanical load, the resistivity matrix is assumed diagonal with equal components ρ_0, i.e. $\rho_1 = \rho_2 = \rho_3 = \rho_0$ and $\rho_4 = \rho_5 = \rho_6 = 0$, being ρ_0 the unstrained resistivity. When an external load is applied, each component of the resistivity matrix varies attending to the piezoresistive behavior of the brick. The resistivity matrices before and after the application of the load, $\boldsymbol{\rho}_0$ and $\boldsymbol{\rho}$, respectively, can be related through:

$$\boldsymbol{\rho} = \boldsymbol{\rho}_0 (\boldsymbol{I} + \boldsymbol{r}) \tag{2}$$

here, the term $\boldsymbol{r}$ stands for the relative change in resistivity defined as $\boldsymbol{r} = \boldsymbol{\Pi}\boldsymbol{\varepsilon}$, with $\boldsymbol{\varepsilon}$ being the strain matrix originated by the external load. The components of the resistivity matrix $\boldsymbol{\rho}$ can be written as follows:

$$\begin{bmatrix} \rho_1 \\ \rho_2 \\ \rho_3 \\ \rho_4 \\ \rho_5 \\ \rho_6 \end{bmatrix} = \begin{bmatrix} \rho_0 \\ \rho_0 \\ \rho_0 \\ 0 \\ 0 \\ 0 \end{bmatrix} + \begin{bmatrix} \Delta\rho_1 \\ \Delta\rho_2 \\ \Delta\rho_3 \\ \Delta\rho_4 \\ \Delta\rho_5 \\ \Delta\rho_6 \end{bmatrix} \tag{3}$$

The connection between the relative change in resistivity and the strain matrix is the $\boldsymbol{\Pi}$ matrix whose components are denoted as λ_{ij}. It is hypothesized that smart bricks possess cubic crystal symmetry, similarly to silicon [55], whereby only three $\lambda-$coefficients are needed. Hence, $\boldsymbol{r} = \boldsymbol{\Pi}\boldsymbol{\varepsilon}$ in matrix notation becomes:

$$\begin{bmatrix} \Delta\rho_1/\rho_0 \\ \Delta\rho_2/\rho_0 \\ \Delta\rho_3/\rho_0 \\ \Delta\rho_4/\rho_0 \\ \Delta\rho_5/\rho_0 \\ \Delta\rho_6/\rho_0 \end{bmatrix} = \begin{bmatrix} \lambda_{11} & \lambda_{12} & \lambda_{12} & 0 & 0 & 0 \\ \lambda_{12} & \lambda_{11} & \lambda_{12} & 0 & 0 & 0 \\ \lambda_{12} & \lambda_{12} & \lambda_{11} & 0 & 0 & 0 \\ 0 & 0 & 0 & \lambda_{44} & 0 & 0 \\ 0 & 0 & 0 & 0 & \lambda_{44} & 0 \\ 0 & 0 & 0 & 0 & 0 & \lambda_{44} \end{bmatrix} \begin{bmatrix} \Delta\varepsilon_1 \\ \Delta\varepsilon_2 \\ \Delta\varepsilon_3 \\ \Delta 2\varepsilon_{23} \\ \Delta 2\varepsilon_{13} \\ \Delta 2\varepsilon_{12} \end{bmatrix} \tag{4}$$

where the term λ_{11} represents the piezoresistive effect along one principal crystal axis for co-axial strains (longitudinal piezoresistivity), λ_{12} accounts for the piezoresistive effect along one principal crystal axis for strains applied in a perpendicular crystal axis (transverse piezoresistivity), and λ_{44} describes the piezoresistive effect on an out-of-plane electric field by the change of the in-plane current induced by in-plane shear stress. The experiments conducted by Downey *et al.* [42] evidenced that the piezoresistivity coefficients λ_{11} and λ_{12} are very similar and, therefore, smart bricks are essentially sensitive to volumetric strains (ε_v=$\varepsilon_{11} + \varepsilon_{22} + \varepsilon_{33}$). In addition, it is assumed that, in a similar way to smart concretes doped with carbon nanotubes [56], smart bricks are insensitive to distortion strains what yields λ_{44}=0.

Downey and co-authors also reported that smart bricks exhibit a strong polarization effect [42]. This phenomenon manifests as an inherent time-based drift in the electrical output of the sensors when connected to Direct Current (DC) power sources, that is an increase in their resistance in time. As a solution, it has been reported in the literature that the use of Alternating Current (AC) power sources minimizes this drift [57]. It is also worth noting the biphasic DC measurement technique proposed by Downey *et al.* [58] for resistivity measurements in smart concretes. This technique was also employed in reference [42] for smart bricks, and stable resistance readings were reported with minimal polarization effects. In this light, limiting the theoretical simulations to the steady-state response of the sensors is in line with existing technical possibilities.

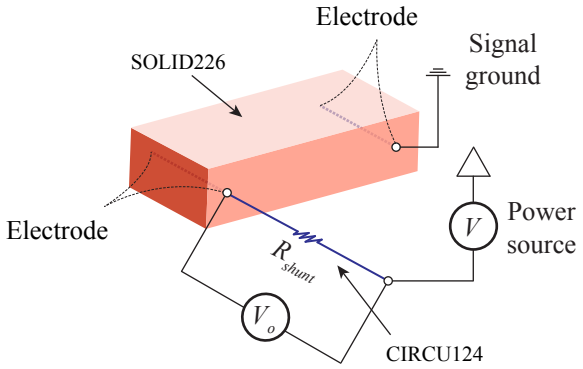

Figure 3: Schematic of resistivity measurement simulation in smart bricks.

On the basis of the previous discussion, Fig. 3 schematizes the simulation of the resistivity measurement setup for smart bricks. The measurement scheme consists of a two-probe resistivity measurement. To this end, two stainless steel wire electrodes are defined embedded symmetrically along the central axis of the brick, and an in-line shunt resistor R_{shunt} is linked between the power source and the first electrode. The smart bricks are modeled with linear piezoresistive SOLID226 elements. These solid elements have twenty nodes and four DOFs per node (three translations and an electric potential). In the simulations, it is assumed that the electrodes can be modeled as a coupling condition of constant voltage along their length and, therefore, they are not explicitly modeled. The shunt resistor is modeled with the general two-nodes circuit element CIRCU124. First, the electric current in the system, I, is obtained by monitoring the voltage drop, V_o, across the in-line shunt resistor, R_{shunt}, as follows:

$$I = \frac{V_o}{R_{shunt}} \tag{5}$$

and, secondly, the resistance between electrodes, R_{int}, is calculated by dividing the voltage difference in the brick, $V - V_o$, by the previously computed current intensity, I, as:

$$R_{int} = \frac{V - V_o}{I} \tag{6}$$

4. Damage detection algorithm based on Kriging interpolation of strain

In this section, a damage detection approach is proposed based on a Kriging interpolation of the electrical output of smart bricks. Firstly, the mathematical formulation of Kriging interpolation is concisely outlined. Afterward, details on its implementation to map the strain field in a masonry structure equipped with a network of smart bricks are provided.

4.1. Kriging interpolation

The Kriging model, with origin in Geostatistics [59], is a commonly used technique of interpolation for spatial data. In this work, the electrical outputs of a set of N smart bricks constitute the observations vector $\mathbf{Y}=[y_1,\ldots,y_N]^T$, while the locations of the sensors in the host structure define the design sites $\mathbf{X}=[\mathbf{x}_1,\ldots,\mathbf{x}_N]$, with $\mathbf{x}_i \in \mathbb{R}^3$ for $i=1,\ldots,N$. The Kriging interpolator conceives the unknown function of interest $y(\mathbf{x})$ at any location $\mathbf{x}$ in the structure, as the sum of a regression model $y_r(\mathbf{x})$ and a random function $\mathcal{F}(\mathbf{x})$ with mean zero as follows [60]:

$$y(\mathbf{x}) = y_r(\mathbf{x}) + \mathcal{F}(\mathbf{x}) \tag{7}$$

It can be understood that $y_r(\mathbf{x})$ globally approximates the design space, whilst $\mathcal{F}(\mathbf{x})$ introduces localized deviations so that the Kriging model interpolates the N-sampled data points. The regression function $y_r(\mathbf{x})$ depends upon p regression parameters, $\boldsymbol{\beta}=\left[\beta_1,\ldots,\beta_p\right]$, and given functions, $\mathbf{f}(\mathbf{x})=\left[f_1(\mathbf{x}),\ldots,f_p(\mathbf{x})\right]$ with $f_i : \mathbb{R}^3 \rightarrow \mathbb{R}$, as [61]:

$$y_r(\boldsymbol{\beta},\mathbf{x}) = \mathbf{f}^T(\mathbf{x})\boldsymbol{\beta} \tag{8}$$

The covariance matrix of $\mathcal{F}(\mathbf{x})$ between any two of the N-sampled data points $\mathbf{x}_i$ and $\mathbf{x}_j$ reads:

$$\mathrm{Cov}\left[\mathcal{F}(\mathbf{x}_i)\mathcal{F}(\mathbf{x}_j)\right] = \sigma^2 \mathbf{R}\left[r(\boldsymbol{\theta}, \mathbf{x}_i, \mathbf{x}_j)\right] \tag{9}$$

where σ^2 stands for the variance of $\mathcal{F}(\mathbf{x})$, and $r(\boldsymbol{\theta}, \mathbf{x}_i, \mathbf{x}_j)$ is a given spatial correlation function between $\mathbf{x}_i$ and $\mathbf{x}_j$ and dependent on $\boldsymbol{\theta}$ correlation parameters. Among diverse possibilities, Gaussian functions are typically used as correlation functions [62]. Finally, the term $\mathbf{R}$ is a N×N symmetric, positive definite matrix with components $R_{ij} = r(\boldsymbol{\theta}, \mathbf{x}_i, \mathbf{x}_j)$.

The relation between the interpolated values $\hat{y}(\mathbf{x})$ of the response $y(\mathbf{x})$ at an arbitrary point $\mathbf{x}$ is defined by the Kriging predictor as follows:

$$\hat{y}(\mathbf{x}) = \mathbf{f}^{\mathrm{T}}(\mathbf{X})\boldsymbol{\beta}^* + \mathbf{r}(\mathbf{x})^{\mathrm{T}}\mathbf{R}^{-1}(\mathbf{Y} - \mathbf{f}^{\mathrm{T}}(\mathbf{X})\boldsymbol{\beta}^*) \tag{10}$$

where $\mathbf{r}(\mathbf{x})$ is a vector containing the correlations between the design sites and $\mathbf{x}$ as:

$$\mathbf{r}(\mathbf{x})^{\mathrm{T}} = [r(\boldsymbol{\theta}, \mathbf{x}_1, \mathbf{x}), \ldots, r(\boldsymbol{\theta}, \mathbf{x}_m, \mathbf{x})]^T \tag{11}$$

Hence, once the regression model and the correlation function are selected, the Kriging interpolator is constructed by selecting adequate regression parameters $\boldsymbol{\beta}^*$ and correlation parameters $\boldsymbol{\theta}$. Firstly, the regression problem $\mathbf{f}(\mathbf{X})\boldsymbol{\beta}^* \approx \mathbf{Y}$ has the generalized least squares solution:

$$\boldsymbol{\beta}^* = \left[\mathbf{f}^{\mathrm{T}}(\mathbf{X})\,\mathbf{R}^{-1}\mathbf{f}(\mathbf{X})\right]^{-1}\,\mathbf{f}^{\mathrm{T}}(\mathbf{X})\,\mathbf{R}^{-1}\,\mathbf{Y} \tag{12}$$

and the variance estimate:

$$\sigma^2 = \frac{1}{\mathrm{N}}\left[\mathbf{Y} - \mathbf{f}^{\mathrm{T}}(\mathbf{X})\boldsymbol{\beta}^*\right]^{\mathrm{T}}\,\mathbf{R}^{-1}\,\left[\mathbf{Y} - \mathbf{f}^{\mathrm{T}}(\mathbf{X})\boldsymbol{\beta}^*\right] \tag{13}$$

Finally, the estimation of the correlation parameters $\boldsymbol{\theta}$ results in a non-linear optimization problem through the maximum likelihood estimator:

$$\max_{\theta_k>0} \Gamma(\boldsymbol{\theta}) = \frac{1}{2}(\mathrm{N}\,\ln\sigma^2 + \ln|\mathbf{R}|) \tag{14}$$

4.2. Damage detection approach based on volumetric strain reconstruction

The proposed damage detection algorithm is organized in four consecutive steps as illustrated in Fig. 4. Let us define a set of N smart bricks deployed into a façade of a masonry building. Following the discussion previously presented in Section 3, it is assumed that smart bricks behave as volumetric strain sensors. Thence, the relative variation of the internal resistance $\Delta R/R_o$ of a sensor can be written as:

$$\frac{\Delta R}{R_o} = \frac{\Delta\rho}{\rho_o} \approx \lambda\varepsilon_v \tag{15}$$

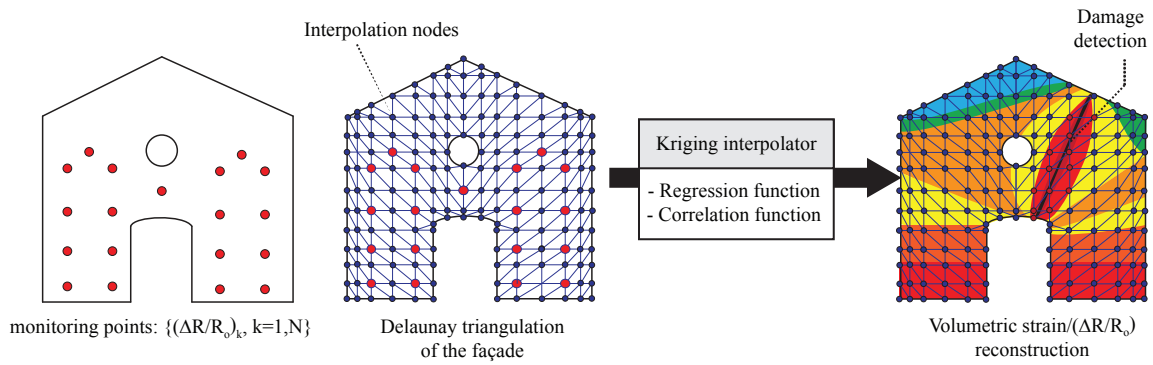

Figure 4: Flowchart of damage detection approach in masonry structures through Kriging interpolation of the measurements of installed smart bricks.

with ΔR the variation of the electrical resistance of the sensor, R_o its electrical resistance in the absence of loads, and λ the piezoresistivity coefficient ($\lambda = \lambda_{11} = \lambda_{12}$), also called gauge factor. From Eq. (15), it is extracted that $\Delta R/R_o$ is directly proportional to ε_v and, thus, can be directly used for damage detection. In this light, the first

step consists of collecting the electrical outputs of the sensors $(\Delta R/R_o)_k$, k=1,...,N. These, along with the spatial locations of the sensors, conform the design sites $\mathbf{X}$ and the observations vector $\mathbf{Y}$, respectively. Subsequently, the monitored façade is discretized by means of Delaunay triangulation so that the interpolation nodes cover uniformly all its surface. Afterward, the observations vector $\mathbf{Y}$ and the design sites $\mathbf{X}$ are utilized to construct the Kriging interpolator. To do so, the DACE Kriging toolbox for Matlab [61] is used considering Gaussian correlation functions and second order polynomial regression functions. Finally, the Kriging interpolator is used to map $\Delta R/R_o$ throughout the whole façade. Once the term $\Delta R/R_o$, or alternatively the volumetric strain ε_v, is reconstructed, it is possible to detect and localize damages through anomalous strain concentrations/releases or load-path modifications.

5. Numerical results and discussion

In this section, two case studies are presented including a masonry shear wall and a three-dimensional masonry building. The first case study is aimed at drawing conclusions about the installation conditions of smart bricks, namely the suitability of the electrical isolation of smart bricks, effects of incorporating smart bricks into a pre-existing structure, and assessment of the correlation between the appearance of damage and the electrical output of the sensors. In the second case study, a masonry building is studied under the action of seismic loadings. Specifically, results of a pushover analysis and direct-time integration of the response under ground acceleration are presented. These numerical tests are aimed at demonstrating the effectiveness of the proposed Kriging interpolation-based damage detection approach. In the remainder of this paper, the material parameters used in the simulations are collected in Tables 1, 2 and 3 for micro-modeling, simplified micro-modeling and macro-modeling approaches, respectively.

Table 1: Electromechanical properties of three-phase micro-modeling of masonry [42, 63] (the elastic modulus of smart bricks is computed through the rule of mixtures considering a $Ti0_2$ concentration of 5 wt.% with Young's modulus of 283 GPa).

	Brick unit	Mortar	Smart brick
Elastic parameters			
Density [kg/m^3]	2100	2162	2154
Elastic modulus [Mpa]	16700	782	23481
Poisson's ratio	0.15	0.14	0.15
Electrical properties			
Gauge factor (λ)	919	-	1804
Resistivity [Ωm]	190	16	117

Table 2: Mechanical properties of simplified micro-modeling of masonry [64, 65].

	Symbol	Value
Brick units		
Magnitude		
Young's modulus [Mpa]	E	8000
Poisson's ratio	ν	0.14
Tensile strength [MPa]	σ_t	2
Cohesion [Mpa]	c	2.8
Friction angle [°]	θ	45
Dilatancy angle [°]	ψ	0
Joints		
Tensile strength [MPa]	f_t	0.25
Mode I fracture energy [J/m^2]	G_f^I	18
Cohesive strength [MPa]	c_o	0.35
Friction angle [°]	θ	36.9
Dilatancy angle [°]	ψ	0
Mode II fracture energy [J/m^2]	G_f^{II}	125
Normal contact stiffness [N/mm^3]	k_σ	82
Tangential contact stiffness	k_τ	36
Opening contact stiffness	k_o	82 (bed) - 82E-4 (head)
Maximum internal friction coefficient	μ	0.75

Table 3: Mechanical properties of macro-modeling of masonry [64, 65].

Elastic parameters	
Density [kg/m^3]	2112
Elastic modulus [Mpa]	3800
Poisson's ratio	0.14
Yield Drucker-Prager criterion	
Cohesion [Mpa]	0.6
Friction angle [°]	36
Dilatancy angle [°]	0
William and Warnke surface	
Compressive strength [MPa]	15
Tensile strength [MPa]	0.35
Shear transfer coefficient for closed cracks (β_c)	0.2
Shear transfer coefficient for open cracks (β_t)	0.2

5.1. Masonry shear wall

The first case study corresponds to the masonry shear wall tested by Velmeltfoort *et al*. [66] and sketched in Fig. 5. The specimen had a width of 99 cm and a height of 100 cm made of 210 mm×100 mm×52 mm solid clay bricks with 10 mm thick mortar. The wall consisted of 18 courses, in which 2 courses were clamped to two steel beams in the bottom and upper parts of the wall. With regard to the loading conditions, the specimen was first subjected to a pre-compression distributed load of 0.3 MPa at the top. Subsequently, three vertical jacks were used to maintain the horizontal position of the upper steel beam and, finally, a monotonically increasing horizontal load F was applied to the top beam. In this work, four smart bricks are defined inserted into the specimen and labeled as SB-i with i=1,...,4 as shown in Fig. 5.

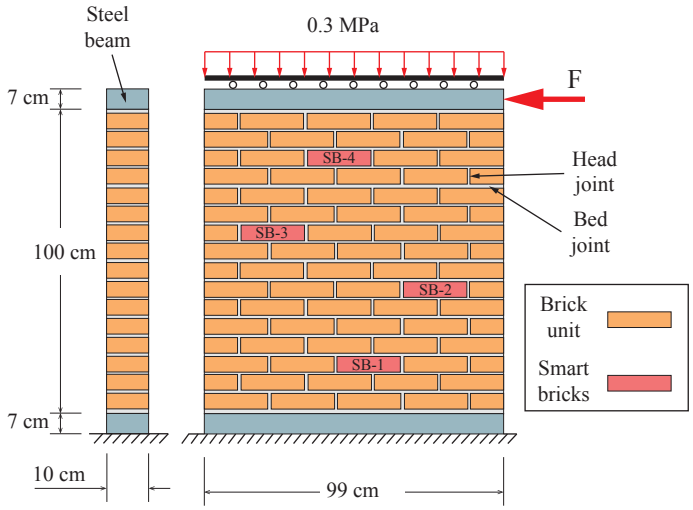

Figure 5: Schematics of masonry shear wall equipped with four smart bricks (SB-i, i=1,...,4).

Firstly, the numerical tests are aimed at investigating the operating conditions of the monitoring system, including the suitability of electrically isolating the smart bricks, and their installation into pre-existing structures. For this purpose, a detailed micro-modeling approach is necessary (Fig. 2(a)) to properly define the electrical problem, assigning different electrical properties to brick units and mortar. In practice, the installation of smart bricks would be conducted in a healthy structure prior to the appearance of damage or, conversely, in an undamaged section of the host structure to guarantee a proper strain transfer. Because of this, and in order to limit the computational cost and mesh density, a three-phase micro-model is defined considering the electromechanical properties from Table 1. It is noted the brick-mortar interaction is neglected for simplicity purposes, and only small loading levels are applied to ensure that the wall remains elastic. Fig. 6 shows the developed FE model of the masonry shear wall equipped with four smart bricks. In this case, the steel beams are not explicitly modeled but their effect is accounted for through appropriate boundary conditions. The electrical output of each sensor is assessed by a two-probe resistivity measurement setup as previously indicated in Section 3. Moreover, considering the high electrical conductivity of the steel beams, it is assumed that the bottom face of the wall is grounded (0 V), while the voltage level in the upper face is defined constant through a coupling equation of its voltage DOFs.

It is also considered that the passive electrodes of the bricks are commonly grounded to the base, while potential differences of 10 V are applied to the active electrodes. With regard to the mechanical boundary conditions, the three translational DOFs are constrained at the bottom support to simulate a pin condition. Following the considerations of Lourenço [44], it is assumed that the upper steel beam stayed in horizontal position during the tests and, therefore, rollers are placed on top to constraint the vertical displacements.

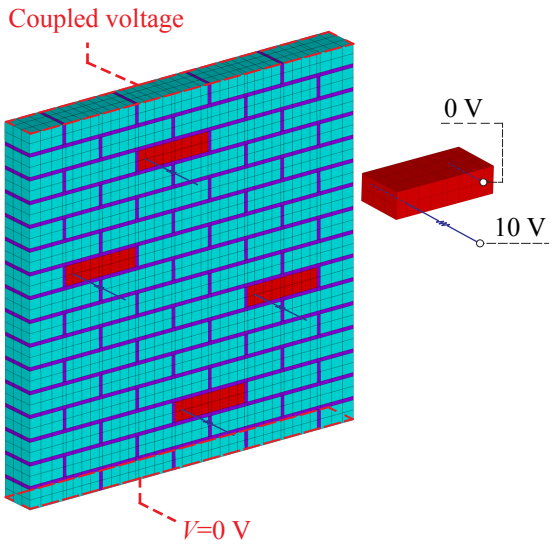

Figure 6: Three-phase micro-model of masonry shear walls with smart bricks.

Fig. 7 presents the distributions of voltage and conduction current density throughout the shear wall in absence of mechanical loads, when a voltage difference of 10 V is applied to each smart brick for electrically isolated and non-isolated conditions. In this analysis, it is considered that both neat and smart bricks are piezoresistive with electromechanical properties taken from Table 1. Moreover, in order to simulate conditions of electrical isolation in Fig. 7 (b), it is assumed that the electrical resistivity of mortar and neat bricks is 1E+6 times that of the smart bricks. In this case, it is observed that the highest voltage gradients are found between the electrodes and, accordingly, the current only flows across the smart bricks. Conversely, when the smart bricks are not isolated (Fig. 7 (a)), the active volume, characterized by the current flow, is not limited to the smart bricks themselves, but also involves surrounding mortar layers and bricks what agrees with the experimental evidence in reference [42].

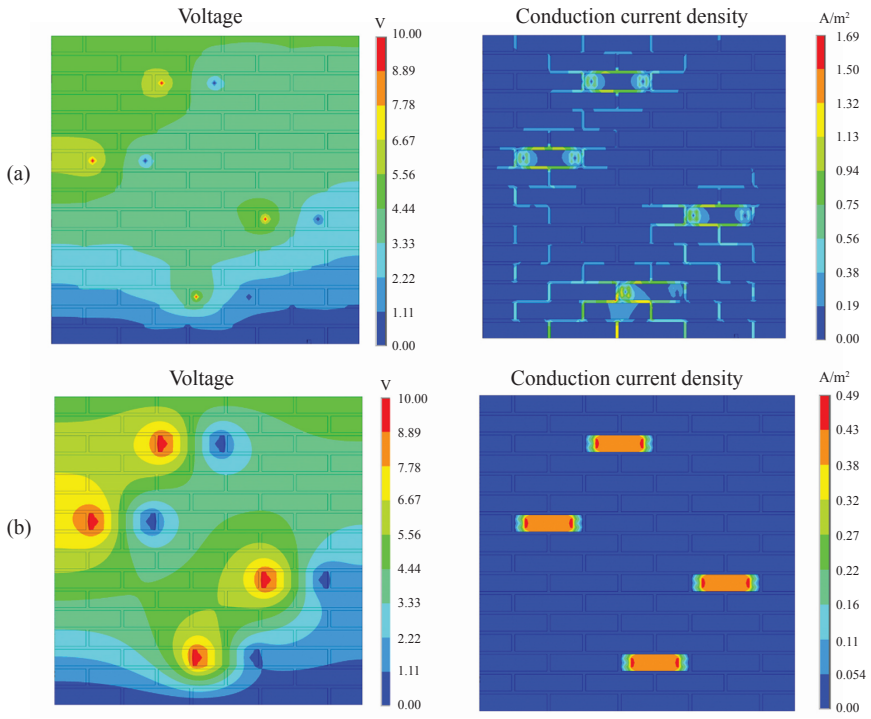

Figure 7: Distributions of voltage and conduction current density with (a) electrically non-isolated smart bricks and (b) isolated smart bricks.

In order to evaluate the influence of isolation conditions on the electrical output of the sensors, a vertical pre-compression of 0.3 MPa and a lateral load of 10.8 kN are applied to the shear wall. It is important to note that, according to the experimental results in reference [66], the masonry wall remains elastic for such load level. For clarity purposes, the load cases have been labeled from LC-1 to LC-4, including the application of the power supply (LC-1), the application of the vertical pre-compression (LC-2), definition of rollers in the upper part of the wall (LC-3), and the application of the lateral load (LC-4). Figs. 8 (a) and (b) depict the electrical current outputted by the smart sensors for electrically isolated and non-isolated conditions, respectively. The results obtained for load case LC-2 have been omitted for clarity purposes since they coincide with those for LC-1. In the case of electrically isolated smart bricks in Fig. 8 (a), it is observed for LC-1 that all the sensors output the same current as expected given that no mechanical loads are applied. Once the vertical compression is applied, i.e. LC-3, the electrical current across the sensors experiences a notable increase attending to the piezoresistive behavior of the smart bricks. In particular, smart bricks SM-1 to SM-4 yield descending currents, a fact that matches the decreasing strain, ε_{zz}, along the wall's height and the location of the sensors (see Fig. 5). In the last load case, LC-4, the electrical current of the sensors decreases as a result of the tension strut originated as a result of the application of the lateral load. Moreover, sensors SM-2 and SM-3 yield lower currents than those outputted by sensors SM-1 and SM-4, a behavior that can be extracted from the shear strain state of the wall and the location of the sensors. On the other hand, it is observed in Fig. 8 (b) that the electrical currents computed for electrically non-isolated conditions are substantially larger. The reason for such behavior, in accordance with the previously reported results in Fig. 7, lies in the possibility of current to flow through the adjacent mortar layers (which are considerably more conductive that clay bricks) as well as through the rest of the bricks. In addition, it is observed that the strain state cannot be readily traced from the electrical output. In this case, smart sensors SM-1 and SM-2 yield considerably larger electrical currents in all the load cases. The reason for such behavior is ascribed to the piezoresistive behavior of neat bricks which, after the application of the vertical compression, induce a highly conductive region in the bottom section of the shear wall.

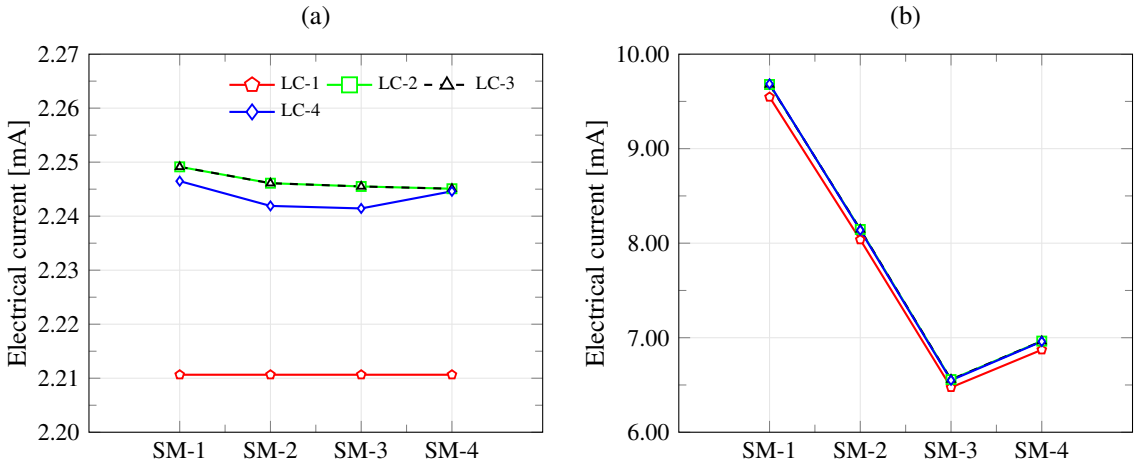

Figure 8: Electrical current outputted by the smart sensors deployed into the shear wall under electrically isolated conditions (a), and non-isolated conditions (b) LC-1 stands for the load case corresponding to the application of the power supply, LC-2 the application of the vertical pre-compression, LC-3 the definition of rollers in the upper part of the wall, and LC-4 the application of the lateral load).

In order to further the previous analysis, Fig. 9 depicts the relative variation of internal electrical resistance, $\Delta R/R_o$, for electrically isolated and non-isolated conditions versus resulting horizontal and vertical forces. Firstly, it is clearly observed in Figs. 9 (c) and (d) that electrically non-isolated conditions lead to less sensitive sensors. In the case of electrically isolated conditions, it is observed in Fig. 9 (a) that the shear forces induce increases in the electrical resistance of the sensors in accordance with the previously shown results in Fig. 8. Conversely, in the case of electrically non-isolated conditions in Fig. 9 (b), it is observed that the smart sensor SM-1 exhibits a decreasing electrical resistance for increasing horizontal loads. The reason for such behavior is ascribed to the piezoresistive behavior of the surrounding neat bricks which interfere in the electrical output of the sensors. Overall, it can be concluded that both isolation conditions offer strain-sensitive solutions apt for damage detection applications. Nevertheless, due to the interferences introduced in the electrical output of the sensors by conductive mortar and piezoresistive neat bricks, non-isolated smart bricks offer limited potential for strain mapping applications.

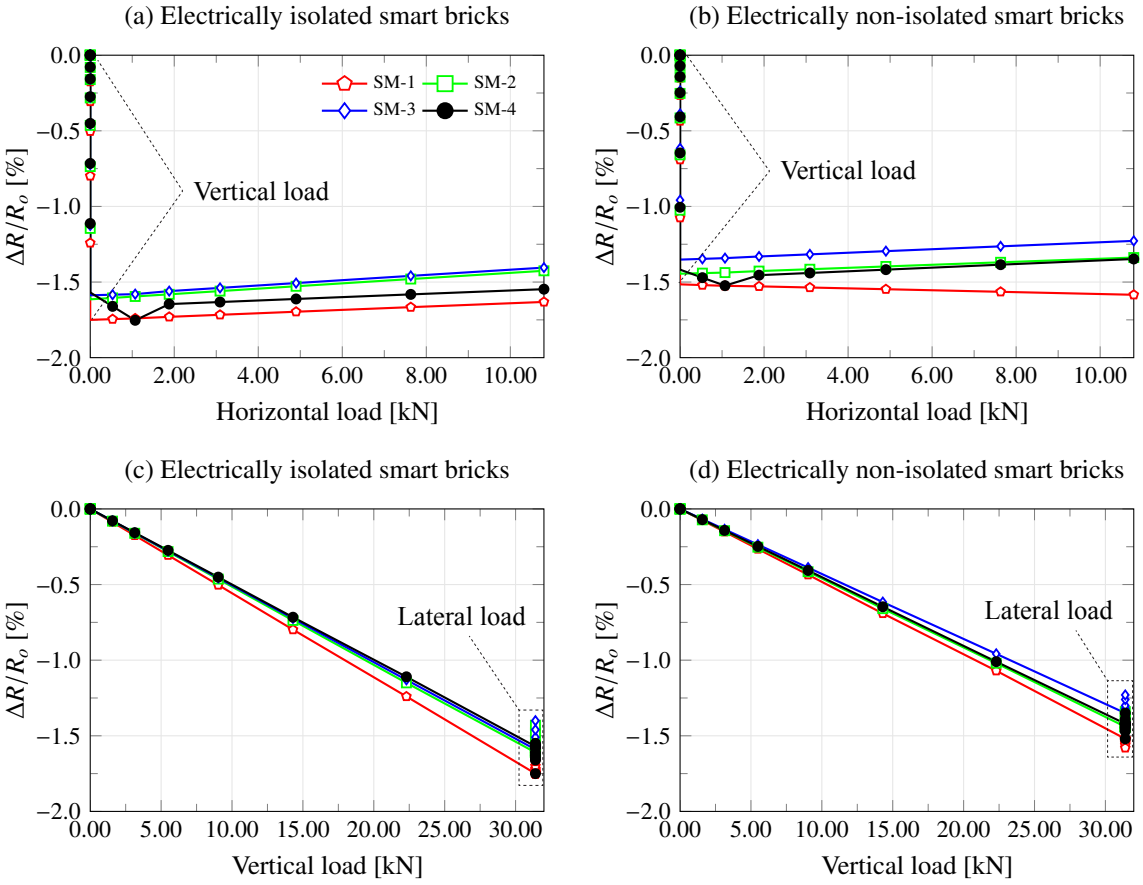

Figure 9: Relative variation of internal resistance $\Delta R/R_o$ of smart bricks deployed into a masonry shear wall for electrically isolated (a,c) and non-isolated (b,d) conditions.

The influence of deployment of a smart brick into the pre-compressed masonry wall is investigated in Figs. 10 and 11. To do so, it is assumed that the smart brick SM-1 is inserted into the wall after the application of the vertical pre-compression (LC-2). On the basis of the previous discussion, the smart bricks are assumed electrically isolated. The simulation of the installation of the smart brick is conducted by the "birth and death" feature in ANSYS, which allows for the deactivation (death) and reactivation (birth) of the stiffness contribution of a group of elements. Fig. 10 furnishes the sequence of vertical strains (ε_{zz}) and electric potentials at the end of the different load cases LC-1 to LC-4, including the installation of SM-1 after LC-2. Firstly, it is observed that SM-1 is free of strain before the application of the lateral load (c). Once the lateral load is applied to the wall, SM-1 begins sustaining strain. It is observed in Fig. 10 (d) that, although there are some disturbances in the strain field due to its posterior incorporation, SM-1 is sustaining strain apt for strain-sensing applications. This analysis is furthered in Fig. 11 by studying the relation between the relative variation of the electrical resistance of the sensors versus the applied horizontal load. It is noted that the strain-sensing curve corresponding to SM-1 directly starts at zero, what reflects its unstrained state when installed. However, as the lateral load is applied, SM-1 exhibits a similar sensitivity if compared to the rest of the sensors. Therefore, it is concluded that smart bricks are suitable for tracking variations in the strain state of pre-existing masonry structures. In the numerical model, perfectly bonded contact conditions are assumed between SM-1 and the surrounding mortar. In practice, it is paramount to ensure that variations in the strain state, and therefore the origin of potential damages, can be effectively transmitted to the smart bricks. Hence, the presented results support the convenience of employing expansive mortars to guarantee a reliable transmission of strains to smart bricks installed into pre-existing structures.

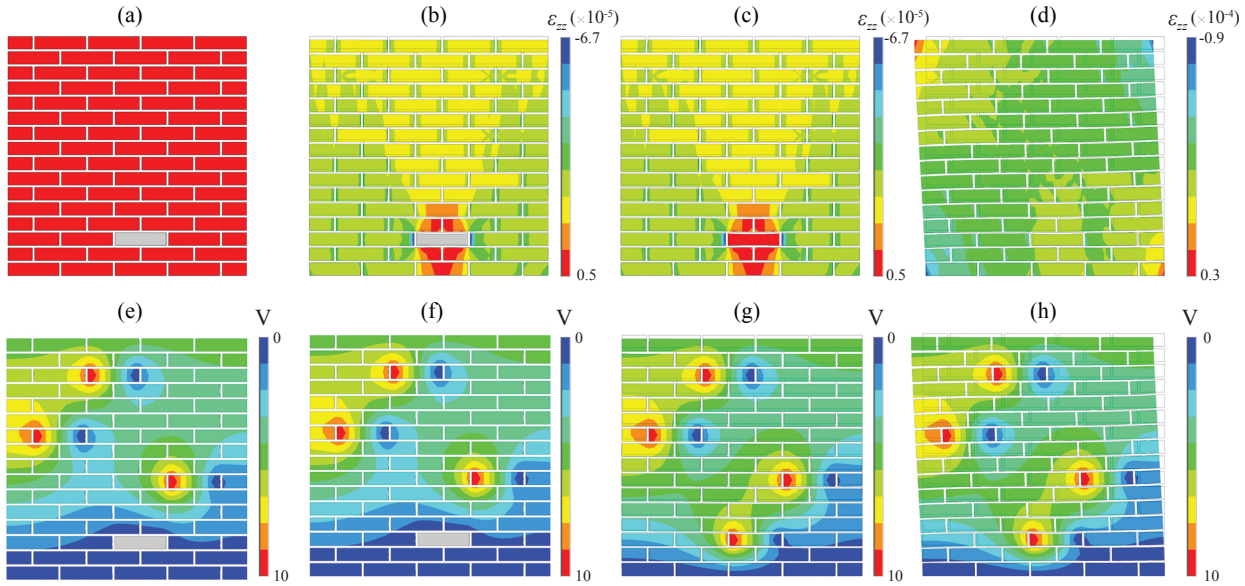

Figure 10: Vertical strain and voltage distribution in masonry shear wall when smart brick SB-1 is deployed after the application of the vertical load at different load steps: (a,e) application of power source in smart bricks deployed into the unstressed shear wall (LC-1), (b,f) application of pre-compression (LC-2), (c,g) deployment of smart brick SB-1, and (d,h) application of lateral loading (LC-4) (smart bricks are assumed electrically isolated).

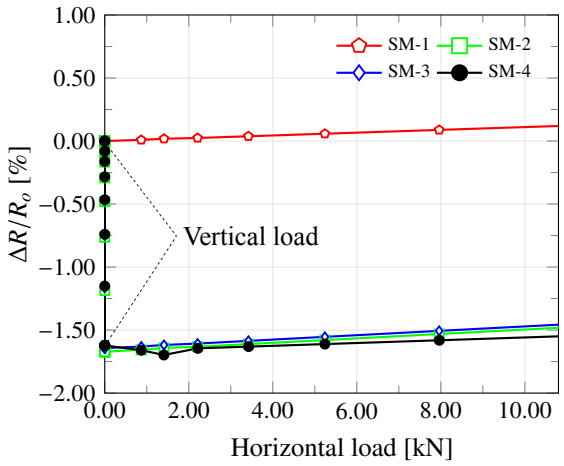

Figure 11: Load-displacement curve at top edge of masonry wall (electrically isolated conditions are assumed for the smart bricks).

In the following, the lateral load is increased up to the failure of the shear wall. In this case, the detailed micro-modeling approach is no longer used because the correct tracking of cracks would require a considerably fine mesh, as well as a high number of contact elements to simulate debonding and sliding failures of unit-mortar interfaces. Instead, the simplified micro-modeling and macro-modeling approaches are used hereafter with the material parameters taken from Tables 2 and 3. In the first place, the numerical simulations are benchmarked against the experimental results reported in reference [66] in terms of horizontal loads and displacements at the top edge of the masonry wall in Fig. 12. Additionally, the computed lateral displacements and crack patterns are depicted in Fig. 13. It is observed that both approaches provide reasonably good agreements with the experimental results, as well as similar crack patterns as those observed experimentally. In the case of the simplified micro-modeling approach, bending horizontal cracks firstly propagate in the top left corner and the bottom right corner. Subsequently, a number of vertical and horizontal joints starts failing in the center of the wall. Eventually, the compression diagonal suddenly splits open forming a step-wise diagonal crack and leading to a drop off in load. During this process, the bending cracks temporarily become inactive as they are closing. In the case of the macro-modeling approach, it is not possible to track the failure of the unit-brick interfaces and, as a result, higher differences are found with the experimental data in Fig. 12. In the experiments, no brittle drop was reported but

a residual flat curve stemming from a softening behavior of the crushed elements in the top right and bottom left corners. The origin of the drop off in load is thus ascribed to the consideration of the elastic-perfectly plastic Drucker-Prager model. Nonetheless, this work is aimed at investigating the application of smart bricks to detect the appearance of damages and, therefore, the post-failure response is secondary. The employed modeling approaches are thus considered suitable for the purpose of this work. A further discussion on the comparison of different modeling approaches can be found in reference [67].

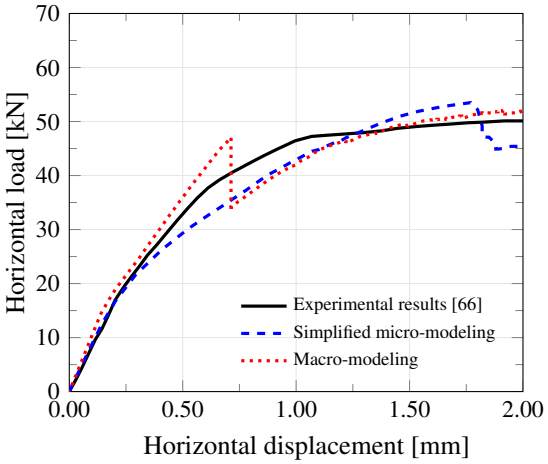

Figure 12: Comparison of experimental load-displacement curve at top edge of the masonry shear wall with simplified micro-modeling and macro-modeling approaches.

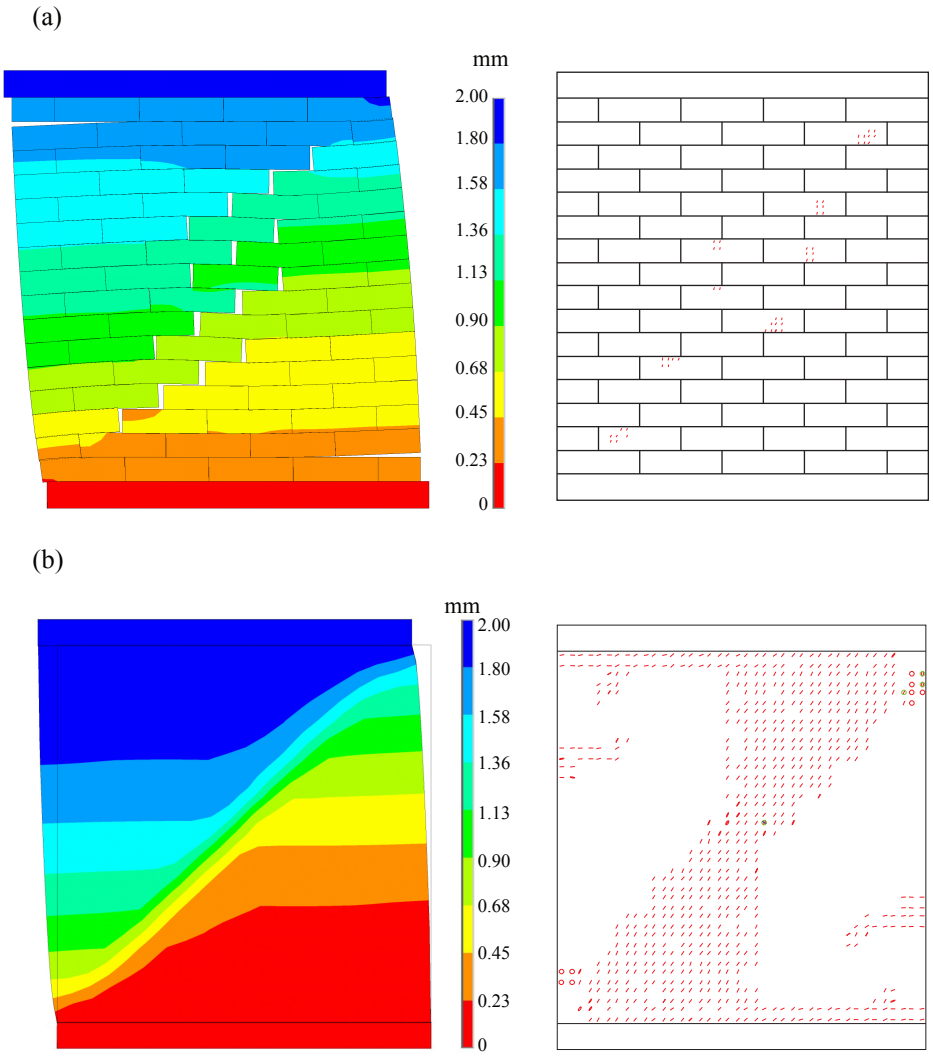

Figure 13: Lateral displacements and crack patterns in the masonry shear wall computed by the simplified micro-modeling (a) and macro-modeling approaches (b).

Figs. 14 and 15 investigate the electrical output provided by the smart bricks deployed into the masonry shear wall subjected to increasing lateral loads up to failure. To do so, the previously introduced simplified micro-modeling approach is used. It is important to note that the smart bricks remain elastic (see Fig. 13 (a)), what is consistent with the formulation of piezoresistive elements SOLID226. Additionally, it is assumed that the smart bricks are electrically isolated and installed into the wall before the application of the pre-compression. Firstly, Fig. 14 represents the horizontal displacements in the wall and current intensities outputted by the sensors versus the simulation time from 0 to 90. It is noted that the simulations have been conducted by a displacement-controlled Newton-Raphson nonlinear analysis, for which time is simply an arbitrarily defined counter to monitor the solution. These results illustrate the simulation process, including the supply of the power source LC-1, the application of the vertical pre-compression LC-2 which corresponds to the linear ascending current intensities in the sensors, an horizontal section corresponding to the application of the rollers to the top beam LC-3 and, finally, the application of the lateral load LC-4. It is noted that the appearance of the diagonal crack in the wall originates disturbances in the electrical signals. Fig. 15 furthers this analysis plotting the relative variation of electrical resistance of the smart bricks versus the horizontal displacements at the top edge of the shear wall. It is observed that the failure process can be readily traced through the electrical measurements in the smart bricks and, therefore, it is possible to conduct damage detection and localization.

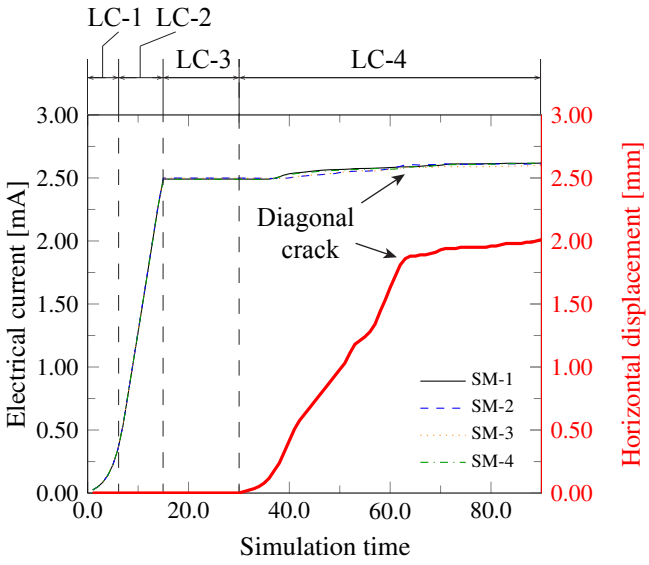

Figure 14: Electrical current and horizontal displacement versus simulation time for electrical isolated smart bricks deployed into the shear masonry wall.

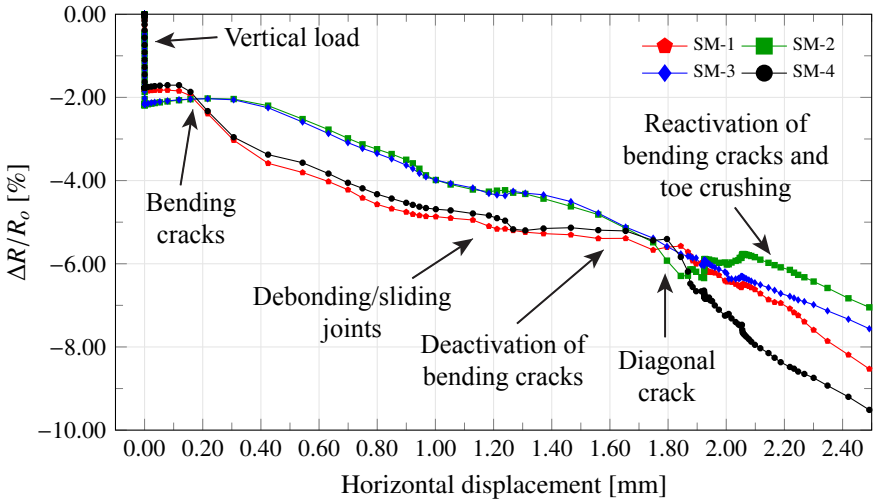

Figure 15: Relative variation of the internal resistance of smart bricks versus horizontal displacements at top edge of the masonry shear wall.

5.2. Masonry building under seismic actions

In this last set of analyses, the proposed Kriging interpolation-based damage detection algorithm is tested in a three-dimensional three-story masonry building. The plan layout is made of a single cell with outer dimensions of 7×5 m as shown in Fig. 16, while the inter-story heights measure 3.2 m. A 1 m high parapet wall is present on the third floor, so the total height of the building is 10.6 m. The masonry walls have a constant thickness of 0.40 m. Each floor is assumed to impose a rigid diaphragm condition at each floor level and an added weight of 5 kN/m^2. Finally, the building is constructed on a perimeter reinforced concrete beam of 0.4 m.

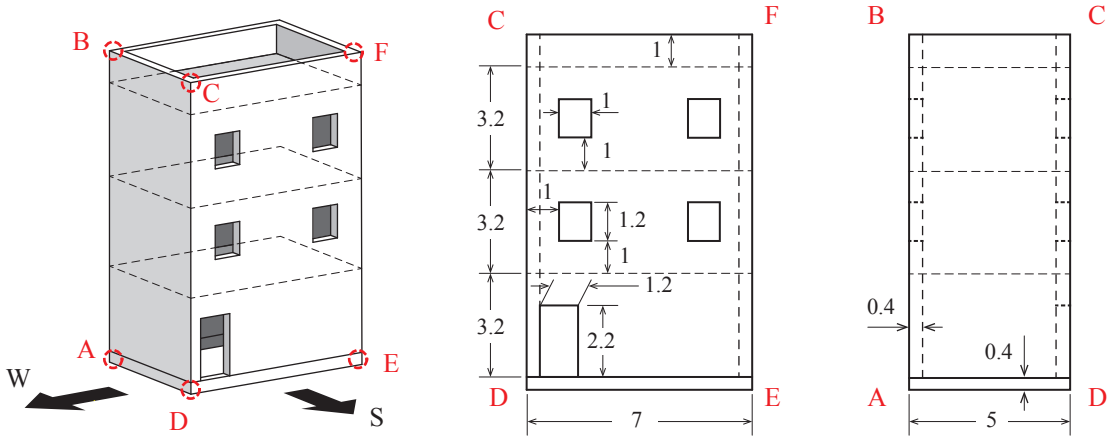

Figure 16: Plan dimensions of the three-dimensional masonry building (units in m).

Using the FE code ANSYS, a 3D numerical model of the building is created by the macro-modeling technique with material properties taken from Table 3. Point element masses MASS21 are inserted at each floor to model the additional masses. In light of the previous discussion on the installation of smart bricks, it is assumed that the sensors are electrically isolated and installed prior to the application of loads. Hence, and considering that the electromechanical response of piezoresistive materials is in essence non-coupled (the mechanical problem determines the electrical one but and not vice versa), the smart bricks are not explicitly modeled in this case study. All in all, the final numerical model consists of 12519 nodes and 7616 SOLID65 elements.

The model is preliminary used to evaluate the modal shapes through a modal analysis. Results show that the first mode shape is a first bending mode in the W-E direction with frequency 7.80 Hz, the second one is a first bending mode in the N-S direction with frequency of 9.08 Hz and, finally, the third one is a torsional mode with frequency equal to 16.96 Hz.

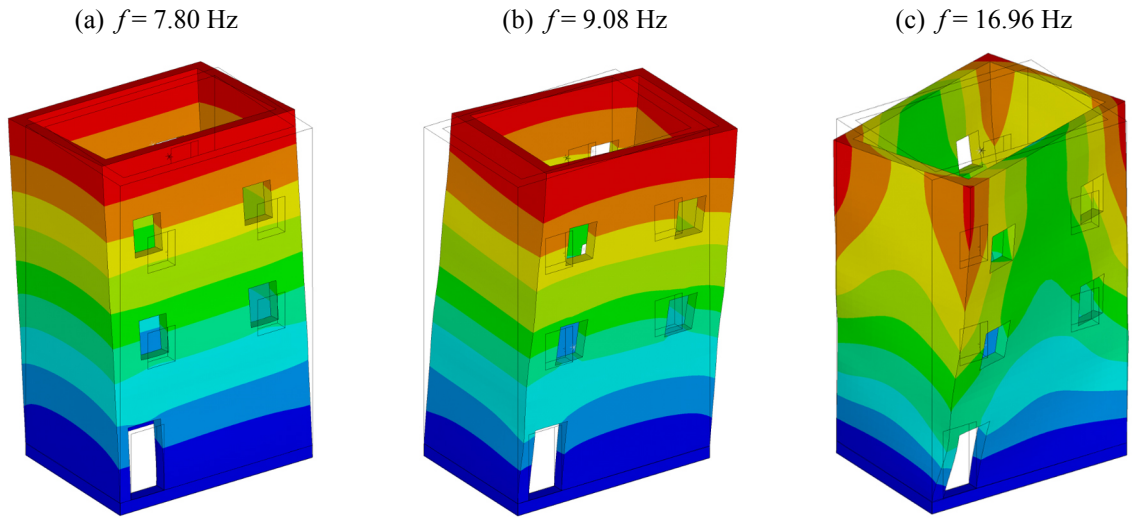

Figure 17: First three numerical modes of vibration of the three-dimensional masonry building.

In the following, two different studies are conducted, namely a pushover analysis and a direct-time integration of the response of the building under ground accelerations.

5.2.1. Pushover analysis

The FE model is first used to perform a pushover analysis in the E-W direction. To do so, a displacement-controlled nonlinear analysis is performed considering a distribution of forces at each floor level proportional to the second mode shape (bending in the E-W direction). Fig. 18 reports the crack pattern obtained at the last step of the analysis. The predicted damage pattern is a combination of shear and flexural cracks. Diagonal cracks are

present in the south façade crossing the windows in the second and third floors, as well as at the lintel of the door. In addition, a vertical crack starts at the corner labeled “A”, and shear cracks take place in the base of the building in contact with the concrete beam. Finally, three horizontal cracks can be also observed crossing completely the west façade.

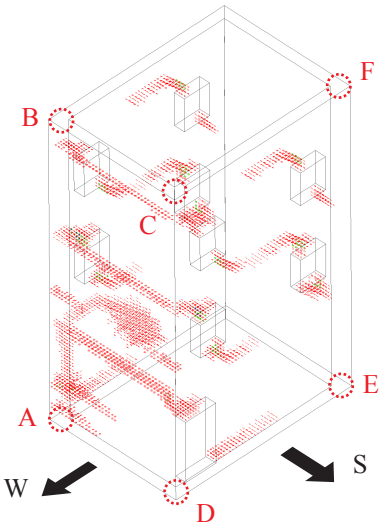

Figure 18: Computed crack pattern in the three-dimensional masonry building for a pushover analysis in the N-S direction.

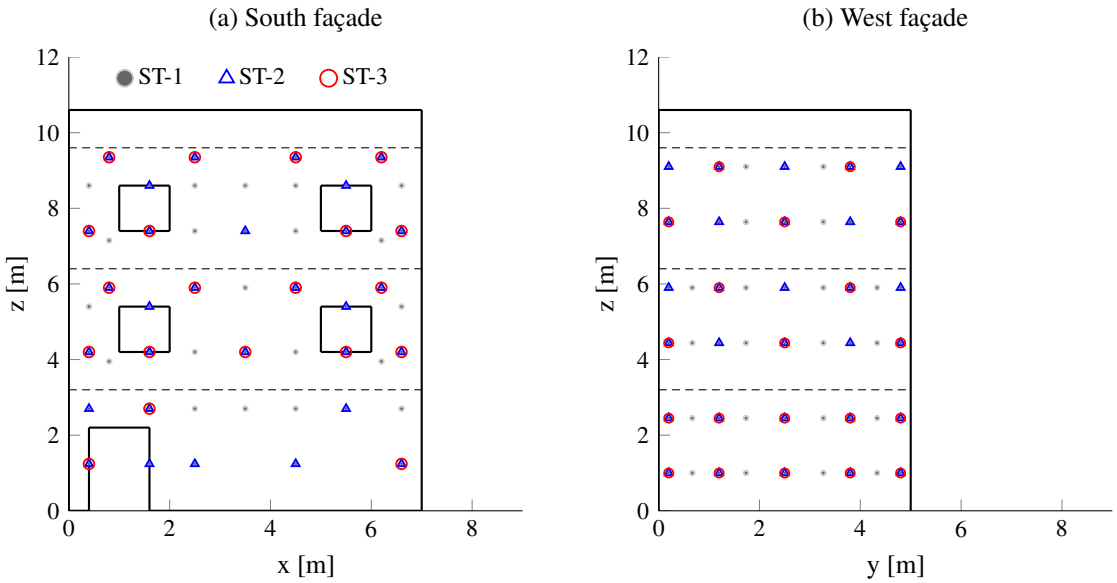

Figure 19: Measurement setups on south and west façades consisting of 20 (ST-1), 30 (ST-2) and 50 (ST-3) smart bricks.

In order to evaluate the potential application of smart bricks for SHM of the masonry building, three different measurement setups are defined as shown in Fig. 19. Particularly, these include 20, 30 and 50 smart bricks inserted in the south and west façades and labeled with ST-1, ST-2 and ST-3, respectively. The pushover analysis is conducted in three consecutive load steps, namely the application of dead loads (P-LC-1), application of lateral loads (P-LC-2), and removal of lateral loads (P-LC-3). In this way, it is intended to investigate the influence of the number of sensors, as well as the potential of the proposed approach to detect and localize damages in the structure with different loading conditions. On this basis, Fig. 20 depicts the Kriging-based reconstruction of the relative variation of the electrical resistance throughout the south façade for the three considered load cases. To do so, the volumetric strain ε_v is monitored at the sensors' positions for the measurements setups ST-1, ST-2 and ST-3. Subsequently, the relative variation of electrical resistance of the sensors is extracted from Eq. (15). Let us recall that the relative variation of electrical resistance of smart bricks is directly proportional to the volumetric

strain and, therefore, both terminologies are used indistinctly in the remainder of the section. Firstly, it is noted that the diagonal cracks cannot be readily observed in LC-3. Conversely, pronounced localized variations in the electrical resistance are clearly observed along the diagonal crack planes in LC-2. In particular, four main diagonal cracks, labeled from C1 to C4, can be clearly identified as strain concentrations at the left windows' corners and the left side of the lintel of the door. Once the lateral loads are removed in LC-3, the originated diagonal cracks close and the compressive strains can be transferred across the crack planes. The maps of relative variations of electrical resistance in LC-3 are also indicative of this as there exists a notable asymmetry. Specifically, there are observable concentrations around the right window in the second floor, a fact that reflects a load-path change with compressive strain releases in the left side of the façade. With regard to the influence of the number of sensors, it is observed that the resolution of the strain reconstructions is increasing with the number of sensors. In particular, the diagonal cracks in the windows, C1 to C3, can be detected by the three measurement setups, while crack C4 goes unnoticed by ST-1.

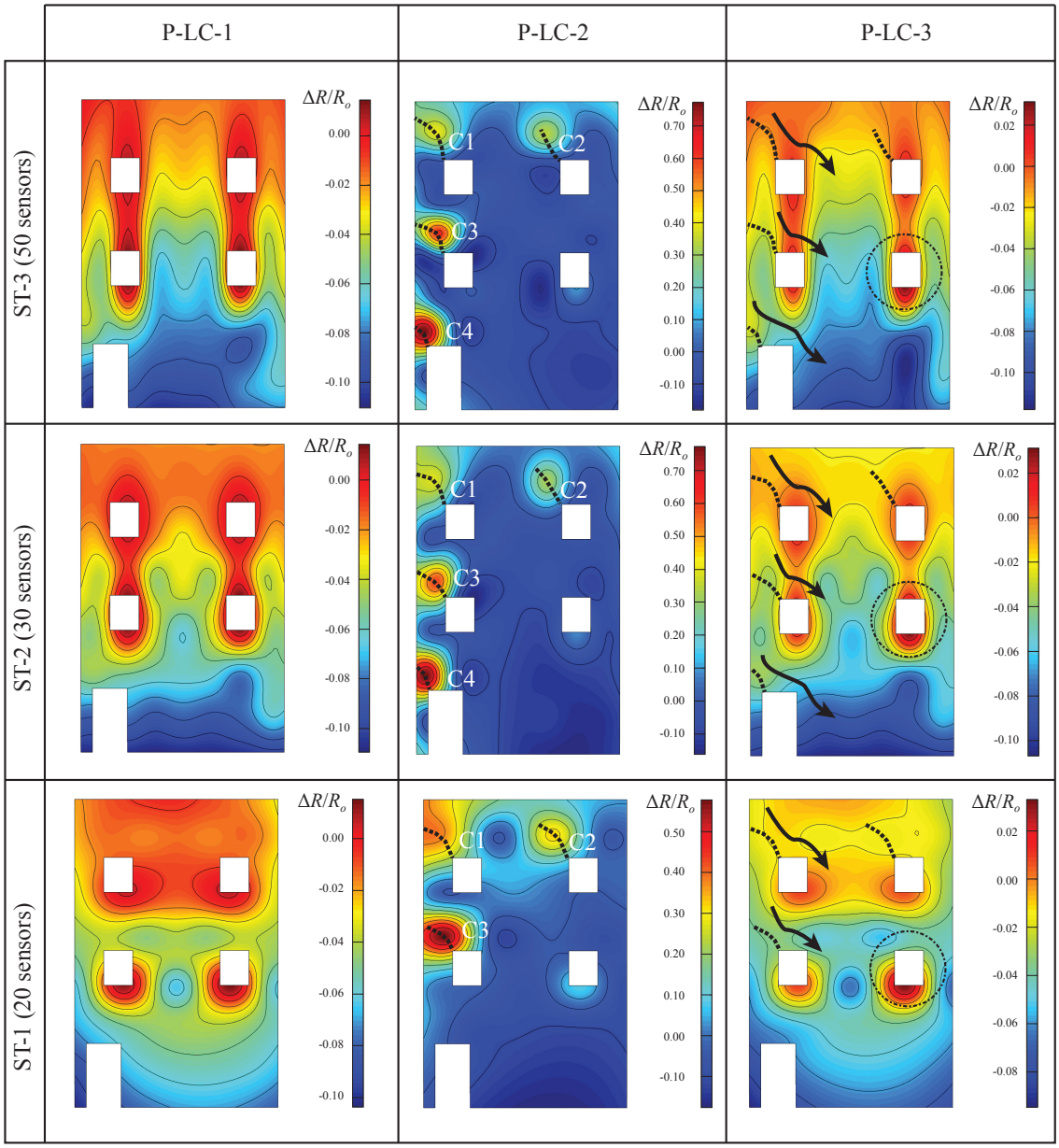

Figure 20: Relative variation of electrical resistance reconstructed by the Kriging interpolation for a pushover analysis of the 3D masonry building in the E-W direction. (ST-1, ST-2 and ST-3 stand for measurement setups considering 20, 32 and 50 smart bricks. P-LC-1, P-LC-2 and P-LC-3 denote the pushover load cases consisting of application of dead loads, lateral loads and release of lateral loads, respectively).

5.2.2. Direct time integration

Finally, the proposed damage detection approach is investigated in the case of the 3D masonry building under ground acceleration. For this purpose, Eurocode 8 spectrum-compatible artificial seismic accelerograms are generated and applied in the W-E direction of the building. Structural damping is considered by the classical Rayleigh formulation, with 4% of damping ratios on the first two modes. In addition, three different Peak Ground Accelerations (PGAs) are considered in order to analyze different damage severities, namely 0.19g, 0.20g and 0.22g. The direct-time integration is carried out defining a time step size of 4E-3 s to prevent the sudden appearance of cracks and related convergence issues. Fig. 21 shows the acceleration time series in the ground and the floor levels in the case of PGA=0.19g. In addition, Fig. 22 depicts the base shear forces versus the drifts in the floor levels of the 3D masonry building for the three considered PGAs.

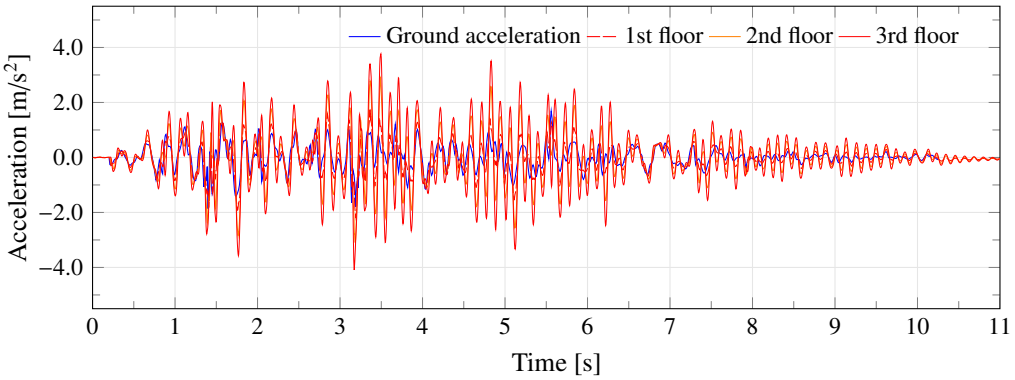

Figure 21: Acceleration time series in the 3D masonry building under ground acceleration with peak acceleration PGA=0.19g.

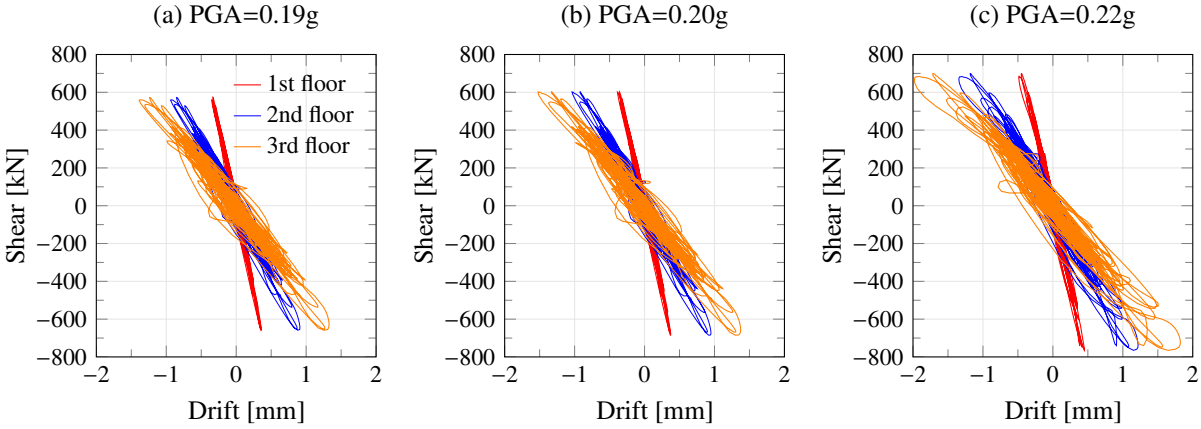

Figure 22: Shear forces versus drifts in the 3D masonry building under ground acceleration with different peak ground acceleration values.

Fig. 23 depicts the Kriging-based reconstruction of the electrical resistance from the output of smart bricks ST-1 to ST-3 (see Fig. 19). These analyses have been conducted at the end of the seismic events and, due to space constraints, no intermediate steps are presented. The computed crack patterns are also depicted in Fig. 23 for both the south and west façades, as well as the three studied PGA values. Firstly, it is observed that the crack pattern is characterized by X-cracks starting in the windows and a vertical/diagonal crack in the door. In addition, horizontal cracks also appear in the west façade extending from the door until the first floor level, the second floor level, and discontinuous horizontal cracks in the second floor. With regard to the maps of variations of electrical resistance, it is first noted that the vertical/diagonal crack in the door is only detected by ST-2 and ST-3. In these cases, a strain concentration is observed in all the load cases. Conversely, this crack goes unnoticed for ST-1 because this counts with no sensor located near this region (see Fig. 19). Interestingly, an increasing asymmetry with the value of PGA is observed for all the measurement setups. With regard to the west façade, the horizontal crack is not easily identifiable in ST-1. The reason for this is due to the closed condition of this crack after the seismic event. Similarly, ST-2 and ST-3 do not show any strain concentration in the crack plane. Nonetheless, an increasing with damage level strain redistribution is clearly observed in these cases. Overall, it is concluded that the proposed

Kriging-based approach provides a valuable tool for interpreting the strain redistribution of damaged masonry structures and, therefore, for damage detection and localization approaches.

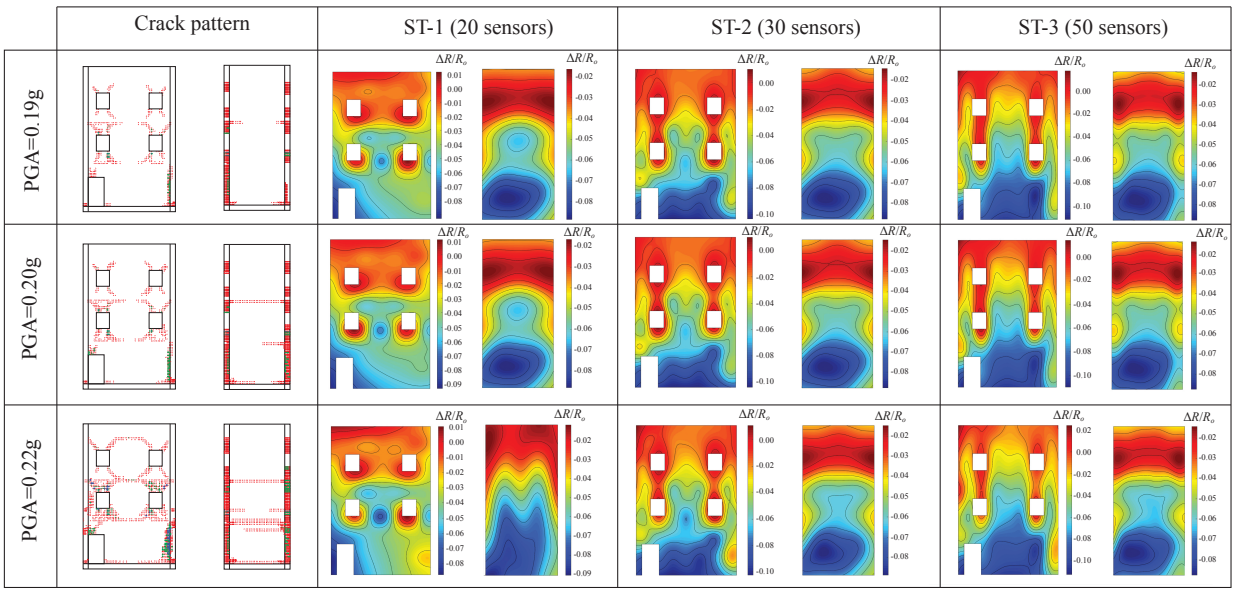

Figure 23: Relative variation of electrical resistance reconstructed by the Kriging interpolation for the direct-time integration of the 3D masonry building under ground accelerations in the E-W direction (ST-1, ST-2 and ST-3 stand for measurement setups considering 20, 32 and 50 smart bricks).

In order to go more into the details of the previous analysis, a damage index D is defined as:

$$D\,[\%] = \frac{R_{dam} - R_{undam}}{R_{undam} - R_o} 100 \tag{16}$$

with R_{dam} and R_{undam} being the electrical resistances of the smart bricks before and after the earthquake, respectively. This index is indicative of the load-path changes induced by damages. A positive value ($D > 0$) indicates load concentration, while a negative value ($D < 0$) reveals load release. In this light, Figs. 24 and 25 represent the index D for the smart sensors in ST-1 deployed into the south and west façades, respectively, and after the earthquake of PGA=0.22g. Furthermore, in order to compute a general metric of the strain redistribution in both façades, the total sum of damage indexes in all the sensors is also indicated. Overall, it is observed that there is a general trend to release strain in the south façade and to increase it in the west one. This fact is in agreement with the damage patterns previously shown in Fig. 23, being the damages concentrated in the façades aligned in the direction of application of the earthquake. In the south façade, it is observed that dead loads tend to concentrate between the windows across the building. In view of this result, X-cracks in the windows are expected, since this could induce the asymmetry in the strain redistribution as previously shown in Fig. 23. It is also noted that the vertical/diagonal crack in the door goes unnoticed because no sensor is located close to it. Nevertheless, the change of sign of the damage index D in the left upper corner of the door indicates the presence of damage in this region. Also, a load release is observed in the left side of the façade towards the west façade, especially in the second and third floors what agrees with the results in Fig. 25. In this case, the presence of an incomplete horizontal crack in the first floor level can be traced through the reported change of sign of the damage index D along the crack plan. Nevertheless, the presence of the rest of the horizontal cracks is hardly identifiable because these remain closed after the earthquake.

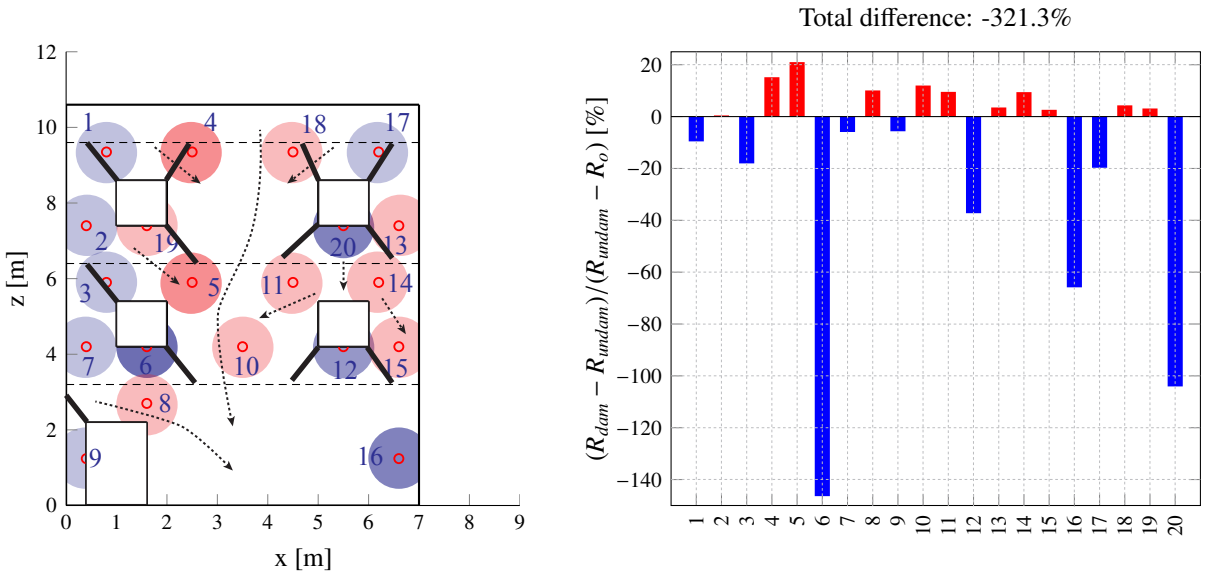

Figure 24: Analysis of the relative variation of electrical resistance of smart bricks deployed into the south façade before and after the appearance of damage (PGA=0.22g in E-W direction, measurement setup ST-1).

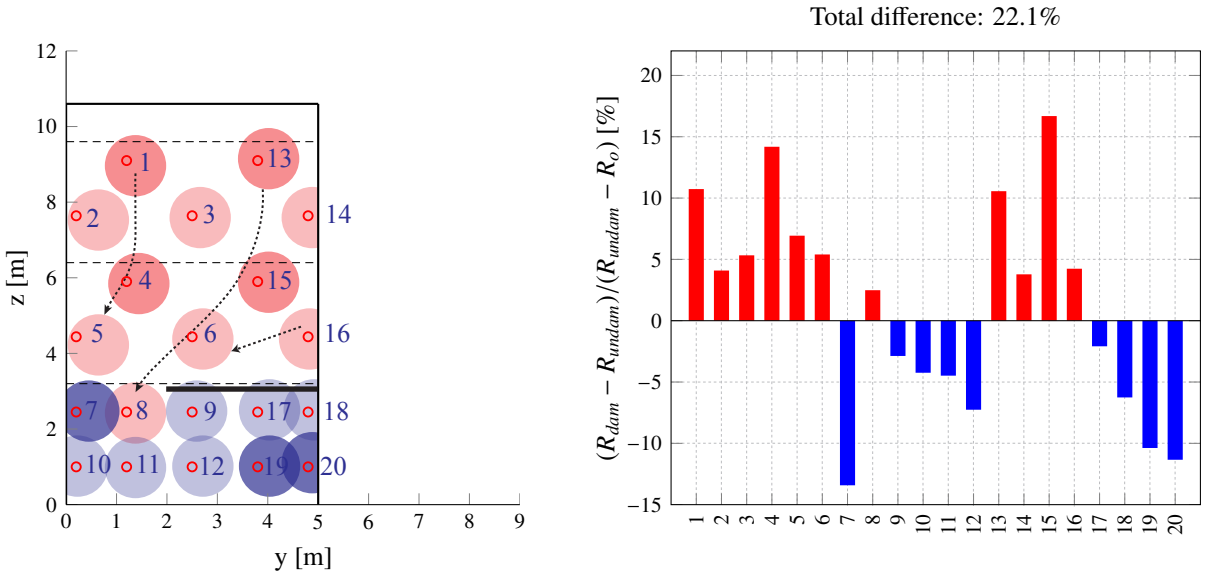

Figure 25: Analysis of the relative variation of electrical resistance of smart bricks deployed into the west façade before and after the appearance of damage (PGA=0.22g in E-W direction, measurement setup ST-1).

6. Conclusions

This paper has presented a theoretical investigation on the application of smart bricks to full-scale masonry structures for seismic assessment. Two case studies, including a masonry shear wall and a 3D masonry building, have been investigated. The first case study has focused on the evaluation of the installation conditions of smart bricks into masonry structures. In particular, the numerical results have investigated the use of electrically isolating the smart bricks from the rest of the structure, and have assessed the effects of installing smart bricks into existing structures. On the other hand, the second case study has assessed the suitability of the proposed Kriging-based strain reconstruction approach for damage detection and localization. To this aim, a pushover analysis and the direct-time integration of the building's response under increasing ground accelerations have been presented.

Firstly, the analysis of the shear wall has demonstrated that isolated smart bricks are more sensitive to mechanical loads. It has been shown that the active flow of current for non-isolated smart bricks also involves regions of the surrounding mortar layers and bricks. Moreover, due to the piezoresistive behavior of neat bricks, the electrical signals outputted by the smart sensors are not limited to local strain effects but average strains surrounding the sensor. The numerical results have also proved that smart bricks installed into pre-compressed structures are suitable to track strain variations. In this case, the piezoresistivity of such sensors is activated when loads different from the initial pre-compression are introduced in the structure. Therefore, smart bricks have been shown to be suitable for damage localization in pre-compressed structures, provided that installation conditions guarantee a correct structure-sensor strain transfer.

Secondly, the analysis of the 3D masonry building under seismic actions has illustrated the potential of the proposed Kriging-based strain reconstruction approach for damage detection and localization. Interestingly, it has been shown that, due to the brittle failure of masonry, the existence of cracks does not necessarily manifest as strain concentrations. In addition, shear and flexural cracks may become inactive after the seismic event so that compressive strains can be transferred through the closed crack planes. As a result, it has been shown that it is paramount to exploit damage-induced variations of the load-paths. For this purpose, a strain redistribution index has been proposed based on the relative variations of the electrical resistance of the sensors after and before the earthquakes. Overall, the numerical results have highlighted the benefits of merging the information of strain redistribution indexes with strain maps for damage detection and localization.

All in all, this paper is envisaged to provide a valuable discussion on the use of smart bricks for generating masonry self-diagnostic structures. Furthermore, the reached conclusions are expected to pave the way for further experimental tests that make it possible to implement this technology to full-scale masonry structures.

Acknowledgment

This work was supported by the Ministerio de Economía y Competitividad of Spain and the Consejería de Economía, Innovación, Ciencia y Empleo of Andalucía (Spain) under projects DPI2014-53947-R and P12-TEP-2546. This paper was also supported by the Italian Ministry of Education, University and Research (MIUR) through the funded project of national interest "SMART-BRICK: novel strain-sensing nanocomposite clay brick enabling self-monitoring masonry structures" (Protocol No. 2015M55L27). E. G-M was also supported by a FPU contract-fellowship from the Spanish Ministry of Education Ref: FPU13/04892.

References

[1] F. Ascione, F. Ceroni, R. F. De Masi, F. de'Rossi, M. R. Pecce, Historical buildings: Multidisciplinary approach to structural/energy diagnosis and performance assessment, Applied Energy 185 (2017) 1517–1528.

[2] M. Anzidei, S. Pondrelli, The Amatrice seismic sequence: preliminary data and results, Annals of Geophysics 59 (2016).

[3] G. Fiorentino, A. Forte, E. Pagano, F. Sabetta, C. Baggio, D. Lavorato, C. Nuti, S. Santini, Damage patterns in the town of Amatrice after August 24th 2016 Central Italy earthquakes, Bulletin of Earthquake Engineering 16 (2018) 1399–1423.

[4] N. Cavalagli, G. Comanducci, C. Gentile, M. Guidobaldi, A. Saisi, F. Ubertini, Detecting earthquake-induced damage in historic masonry towers using continuously monitored dynamic response-only data, Procedia Engineering 199 (2017) 3416–3421.

[5] F. Clementi, A. Pierdicca, A. Formisano, F. Catinari, S. Lenci, Numerical model upgrading of a historical masonry building damaged during the 2016 Italian earthquakes: the case study of the Podestà palace in Montelupone (Italy), Journal of Civil Structural Health Monitoring 7 (2017) 703–717.

[6] M. G. Masciotta, L. F. Ramos, P. B. Lourenço, The importance of structural monitoring as a diagnosis and control tool in the restoration process of heritage structures: a case study in Portugal, Journal of Cultural Heritage 27 (2017) 36–47.

[7] P. Pachón, R. Castro, E. García-Macías, V. Compan, E. Puertas, E. Torrojas bridge: Tailored experimental setup for SHM of a historical bridge with a reduced number of sensors, Engineering Structures 162 (2018) 11–21.

[8] B. Conde, L. F. Ramos, D. V. Oliveira, B. Riveiro, M. Solla, Structural assessment of masonry arch bridges by combination of non-destructive testing techniques and three-dimensional numerical modelling: Application to Vilanova bridge, Engineering Structures 148 (2017) 621–638.

[9] M. Pieraccini, D. Dei, M. Betti, G. Bartoli, G. Tucci, N. Guardini, Dynamic identification of historic masonry towers through an expeditious and no-contact approach: Application to the Torre del Mangia in Siena (Italy), Journal of Cultural Heritage 15 (2014) 275–282.

[10] F. Lorenzoni, F. Casarin, M. Caldon, K. Islami, C. Modena, Uncertainty quantification in structural health monitoring: Applications on cultural heritage buildings, Mechanical Systems and Signal Processing 66 (2016) 268–281.

[11] C. Gentile, M. Guidobaldi, A. Saisi, One-year dynamic monitoring of a historic tower: damage detection under changing environment, Meccanica 51 (2016) 2873–2889.

[12] E. P. Carden, P. Fanning, Vibration based condition monitoring: a review, Structural health monitoring 3 (2004) 355–377.

[13] W. Fan, P. Qiao, Vibration-based damage identification methods: a review and comparative study, Structural health monitoring 10 (2011) 83–111.

[14] L. A. S. Kouris, A. Penna, G. Magenes, Seismic damage diagnosis of a masonry building using short-term damping measurements, Journal of Sound and Vibration 394 (2017) 366–391.

[15] L. F. Ramos, G. De Roeck, P. B. Lourenço, A. Campos-Costa, Damage identification on arched masonry structures using ambient and random impact vibrations, Engineering Structures 32 (2010) 146–162.

[16] M. P. Schuller, Nondestructive testing and damage assessment of masonry structures, Progress in Structural Engineering and Materials 5 (2003) 239–251.

[17] A. Moropoulou, K. C. Labropoulos, E. T. Delegou, M. Karoglou, A. Bakolas, Non-destructive techniques as a tool for the protection of built cultural heritage, Construction and Building Materials 48 (2013) 1222–1239.

[18] E. Verstrynge, K. De Wilder, A. Drougkas, E. Voet, K. Van Balen, M. Wevers, Crack monitoring in historical masonry with distributed strain and acoustic emission sensing techniques, Construction and Building Materials 162 (2018) 898–907.

[19] G. Bartoli, M. Betti, S. Giordano, In situ static and dynamic investigations on the torre grossa masonry tower, Engineering Structures 52 (2013) 718–733.

[20] I. Lubowiecka, J. Armesto, P. Arias, H. Lorenzo, Historic bridge modelling using laser scanning, ground penetrating radar and finite element methods in the context of structural dynamics, Engineering Structures 31 (2009) 2667–2676.

[21] R. Ghorbani, F. Matta, M. A. Sutton, Full-field deformation measurement and crack mapping on confined masonry walls using digital image correlation, Experimental Mechanics 55 (2015) 227–243.

[22] L. Binda, A. Saisi, C. Tiraboschi, Application of sonic tests to the diagnosis of damaged and repaired structures, NDT & E International 34 (2001) 123–138.

[23] E. Z. Kordatos, D. A. Exarchos, C. Stavrakos, A. Moropoulou, T. E. Matikas, Infrared thermographic inspection of murals and characterization of degradation in historic monuments, Construction and Building Materials 48 (2013) 1261–1265.

[24] F. Valvona, J. Toti, V. Gattulli, F. Potenza, Effective seismic strengthening and monitoring of a masonry vault by using Glass Fiber Reinforced Cementitious Matrix with embedded Fiber Bragg Grating sensors, Composites Part B: Engineering 113 (2017) 355–370.

[25] B. Han, S. Ding, X. Yu, Intrinsic self-sensing concrete and structures: A review, Measurement 59 (2015) 110–128.

[26] S. Rana, P. Subramani, R. Fangueiro, A. G. Correia, A review on smart self-sensing composite materials for civil engineering applications, AIMS Materials Science 3 (2016) 357–379.

[27] A. D. B. Ferreira, P. R. Nóvoa, A. T. Marques, Multifunctional material systems: A state-of-the-art review, Composite Structures (2016).

[28] O. Galao, F. Baeza, E. Zornoza, P. Garcés, Strain and damage sensing properties on multifunctional cement composites with CNF admixture, Cement and concrete composites 46 (2014) 90–98.

[29] F. Ubertini, S. Laflamme, A. D'Alessandro, Smart cement paste with carbon nanotubes, Innovative Developments of Advanced Multifunctional Nanocomposites in Civil and Structural Engineering (2016) 97–120.

[30] N. Caterino, I. Iervolino, G. Manfredi, E. Cosenza, Comparative analysis of multi-criteria decision-making methods for seismic structural retrofitting, Computer-Aided Civil and Infrastructure Engineering 24 (2009) 432–445.

[31] J. Wang, L. Zhang, K. Liew, Multiscale simulation of mechanical properties and microstructure of CNT-reinforced cement-based composites, Computer Methods in Applied Mechanics and Engineering 319 (2017) 393–413.

[32] J. Wang, L. Zhang, K. Liew, A multiscale modeling of CNT-reinforced cement composites, Computer Methods in Applied Mechanics and Engineering 309 (2016) 411–433.

[33] R. N. Howser, H. B. Dhonde, Y. L. Mo, Self-sensing of carbon nanofiber concrete columns subjected to reversed cyclic loading, Smart materials and structures (2011).

[34] A. Downey, A. D'Alessandro, M. Baquera, E. García-Macías, D. Rolfes, F. Ubertini, S. Laflamme, R. Castro-Triguero, Damage detection, localization and quantification in conductive smart concrete structures using a resistor mesh model, Engineering Structures 148 (2017) 924–935.

[35] B. Han, B. Han, J. Ou, Experimental study on use of nickel powder-filled portland cement-based composite for fabrication of piezoresistive sensors with high sensitivity, Sensors and Actuators A: Physical 149 (2009) 51–55.

[36] E. García-Macías, A. Downey, A. D'Alessandro, R. Castro-Triguero, S. Laflamme, F. Ubertini, Enhanced lumped circuit model for smart nanocomposite cement-based sensors under dynamic compressive loading conditions, Sensors and Actuators A: Physical 260 (2017) 45–57.

[37] T. Schumacher, E. T. Thostenson, Development of structural carbon nanotube–based sensing composites for concrete structures, Journal of Intelligent Material Systems and Structures 25(11) (2013) 1331–1339.

[38] M. Park, H. Kim, J. P. Youngblood, Strain-dependent electrical resistance of multi-walled carbon nanotube/polymer composite films, Nanotechnology 19 (2008) 055705.

[39] N. Hu, H. Fukunaga, S. Atobe, Y. Liu, J. Li, Piezoresistive strain sensors made from carbon nanotubes based polymer nanocomposites, Sensors 11 (2011) 10691–10723.

[40] F. Avilés, A. I. Oliva-Avilés, M. C. P., Piezoresistivity, strain, and damage self-sensing of polymer composites filled with carbon nanostructures, Advanced Engineering Materials (2018) 1701159.

[41] J. M. Engel, L. Zhao, Z. Fan, J. Chen, C. Liu, Smart brick-a low cost, modular wireless sensor for civil structure monitoring, in: International Conference on Computing, Communications and Control Technologies (CCCT 2004), Austin, TX USA.

[42] A. Downey, A. D'Alessandro, S. Laflamme, F. Ubertini, Smart bricks for strain sensing and crack detection in masonry structures, Smart Materials and Structures 27 (2017) 015009.

[43] J. G. Rots, Numerical simulation of cracking in structural masonry, Heron 36 (1991) 49–63.

[44] P. J. B. B. Lourenço, Computational strategies for masonry structures., Ph.D. thesis, 1997.

[45] M. Sirajuddin, N. S. Potty, J. Sunil, Non linear seismic analysis of masonry structures, Journal of Design and Built environment 9 (2011).

[46] V. G. Haach, G. Vasconcelos, P. B. Lourenço, Parametrical study of masonry walls subjected to in-plane loading through numerical modeling, Engineering Structures 33 (2011) 1377–1389.

[47] P. B. Lourenço, J. G. Rots, Multisurface interface model for analysis of masonry structures, Journal of engineering mechanics 123 (1997) 660–668.

[48] A. Mohyeddin, H. M. Goldsworthy, E. F. Gad, FE modelling of RC frames with masonry infill panels under in-plane and out-of-plane loading, Engineering Structures 51 (2013) 73–87.

[49] K. Chaimoon, M. M. Attard, Modeling of unreinforced masonry walls under shear and compression, Engineering structures 29 (2007) 2056–2068.

[50] T. Li, N. Galati, G. J. Tumialan, A. Nanni, FRP strengthening of URM walls with openings-numerical analysis and design, The Masonry Society Journal (2005).

[51] R. Senthivel, P. B. Lourenço, Finite element modelling of deformation characteristics of historical stone masonry shear walls, Engineering structures 31 (2009) 1930–1943.

[52] G. N. Pande, J. X. Liang, J. Middleton, Equivalent elastic moduli for brick masonry, Computers and Geotechnics 8 (1989) 243–265.

[53] Structural analysis guide, Release 15.0, ANSYS Inc, Cannonsburg, PA (2014).

[54] K. J. William, E. D. Warnke, Constitutive model for the triaxial behavior of concrete, Proceedings of International Association for Bridge and Structural Engineering 19 (1975).

[55] G. K. Johns, Modeling piezoresistivity in silicon and polysilicon, Journal of Applied Engineering Mathematics April 2 (2006) 1–5.

[56] E. García-Macías, R. Castro-Triguero, A. Sáez, F. Ubertini, 3D mixed micromechanics-FEM modeling of piezoresistive carbon nanotube smart concrete., Computer Methods in Applied Mechanics and Engineering, *In press* (2018).

[57] A. Alizadeh Sahraei, M. Ayati, M. Baniassadi, D. Rodrigue, M. Baghani, Y. Abdi, AC and DC electrical behavior of MWCNT/epoxy nanocomposite near percolation threshold: Equivalent circuits and percolation limits, Journal of Applied Physics 123 (2018) 105109.

[58] A. Downey, A. D'Alessandro, F. Ubertini, S. Laflamme, R. Geiger, Biphasic DC measurement approach for enhanced measurement stability and multi-channel sampling of self-sensing multi-functional structural materials doped with carbon-based additives, Smart Materials and Structures 26 (2017) 065008.

[59] G. Matheron, Principles of geostatistics, Economic geology 58 (1963) 1246–1266.

[60] J. Sacks, W. J. Welch, T. J. Mitchell, H. P. Wynn, Design and analysis of computer experiments, Statistical Science (1989) 409–423.

[61] S. N. Lophaven, H. B. Nielsen, J. Søndergaard, DACE-A MATLAB Kriging Toolbox, volume 2, Citeseer, 2002.

[62] J. R. Koehler, A. B. Owen, 9 computer experiments, Handbook of statistics 13 (1996) 261–308.

[63] P. J. Tumidajski, Electrical conductivity of Portland cement mortars, Cement and concrete research 26 (1996) 529–534.

[64] H. B. Kaushik, D. C. Rai, S. K. Jain, Stress-strain characteristics of clay brick masonry under uniaxial compression, Journal of materials in Civil Engineering 19 (2007) 728–739.

[65] T. Taghikhany, M. Tehranizadeh, M. Arabameri, Vulnerability of hybrid masonry building under seismic action, in: The 14th World Conference on Earthquake Engineering. Beijing: Tsinghua University Press.

[66] A. T. Vermeltfoort, T. M. J. Raijmakers, Deformation controlled tests in masonry shear walls, part 2, holandés), Report TUE/BKO/93.08, Eindhoven University of Technology, Eindhoven, Países Bajos (1993).

[67] J. G. Rots, Structural masonry: an experimental/numerical basis for practical design rules, AA Balkema, 1997.